Chromatin modifiers in DNA repair and human disease

Helfricht, A.

LOSS OF ZBTB24, A NOVEL NON-HOMOLOGOUS END-JOINING PROTEIN, IMPAIRS CLASS-SWITCH RECOMBINATION IN ICF SYNDROME

5

IN PREPARATION FOR PUBLICATION

Angela Helfricht[1,#], Peter E. Thijssen[1,#], Hanna IJspeert[2], Rashmi G. Shah[3], Chantal Stoepker[1], Monique M. van Ostaijen-ten Dam[4], Martijn S. Luijsterburg[1], Anton de Groot[1], Rianca Jak[1], Gwendolynn Grootaers[1], Jun Wang[1,‡], Pooja Rao[5], Alfred C.O. Vertegaal[6], Maarten J.D. van Tol[4], Qiang Pan-Hammarström[7], Girish M. Shah[3], Mirjam van der Burg[2], Silvère M. van der Maarel[1] and Haico van Attikum[1]

[1] Department of Human Genetics, Leiden University Medical Center
[2] Department of Immunology, Erasmus Medical Center Rotterdam
[3] CHU de Québec Research Centre (site CHUL), and Université Laval, Laboratory for Skin Cancer Research and Axe Neuroscience, Québec (QC), Canada
[4] Laboratory for Immunology, Department of Pediatrics, Leiden University Medical Center
[5] ServiceXS B.V., Leiden
[6] Department of Molecular Cell Biology, Leiden University Medical Center
[7] Department of Laboratory Medicine, Karolinska Institute, Sweden
[#] Equally contributing authors

ABSTRACT

The autosomal recessive immunodeficiency, centromeric instability and facial anomalies (ICF) syndrome is a genetically heterogeneous disorder. Despite recent successes in the identification of the underlying gene defects, it is currently unclear how mutations in any of the four known ICF genes cause a primary immunodeficiency. Here we demonstrate that loss of ZBTB24 in B cells from ICF2 patients impairs non-homologous end-joining (NHEJ) during immunoglobulin class-switch recombination and consequently impairs immunoglobulin production and subtype balance. Mechanistically, we found that ZBTB24 associates with poly(ADP-ribose) polymerase 1 (PARP1) and stimulates auto-poly(ADP-ribosyl)ation of this enzyme. The zinc finger in ZBTB24 binds PARP1-associated poly(ADP-ribose) chains and mediates the PARP1-dependent recruitment of ZBTB24 to DNA breaks. Moreover, by binding to poly(ADP-ribose) chains ZBTB24 protects these moieties from degradation by poly(ADP-ribose) glycohydrolase (PARG). This enhances the poly(ADP-ribose)-dependent interaction between PARP1 and the LIG4/XRCC4 NHEJ complex and promotes NHEJ by facilitating the assembly of this repair complex at DNA breaks. Thus, we uncover ZBTB24 as a regulator of PARP1-dependent NHEJ and class-switch recombination, providing a molecular basis for the immunodeficiency in ICF syndrome.

INTRODUCTION

Immunodeficiency with centromeric instability and facial anomalies (ICF) syndrome (OMIM 242860; 614069) is a rare autosomal recessive disorder characterized by a triad of phenotypes (Hagleitner et al. 2008; Weemaes et al. 2013). Patients suffer from a variable immunodeficiency, mainly characterized by hypo- or agammaglobulinemia in the presence of B cells, resulting in recurrent and often fatal respiratory and gastrointestinal infections. Furthermore, patients often present with a distinct set of facial anomalies, including a flat nasal bridge, hypertelorism and epicanthal folds. The cytogenetic hallmark of the disease is centromeric instability, specifically at chromosomes 1, 9 and 16, which is associated with CpG hypomethylation of the pericentromeric satellite II and III repeats.

ICF syndrome is genetically heterogeneous and can be subdivided into five different groups (ICF1-4 and ICFX) based on the genetic defect underlying the phenotype (Weemaes et al. 2013; Thijssen et al. 2015). ICF1 patients, comprising approximately 50% of the total patient population, carry mutations in the de novo DNA methyltransferase 3B gene (DNMT3B, ICF1) (Hansen et al. 1999; Xu et al. 1999). Around 30% of the cases carry mutations in the Zinc finger and BTB (bric-a-bric, tramtrack, broad complex) containing 24 gene (ZBTB24, ICF2) (de Greef et al. 2011; Chouery et al. 2012; Nitta et al. 2013). Recently, mutations in the cell division cycle-associated protein 7 (CDCA7, ICF3) or helicase, lymphoid-specific (HELLS, ICF4) were reported in ten patients (~20% of the total patient population), leaving only few cases genetically unaccounted for (ICFX) (Thijssen et al. 2015). Remarkably, however, while the genetic defects underlying ICF syndrome have been largely elucidated, it remains largely unclear how these defects lead to ICF syndrome, in particular the associated life-threatening immunodeficiency.

Interestingly, the number of circulating B-lymphocytes in ICF patients is normal, but a lack of switched memory B cells and an increased proportion of immature B cells have been reported (Blanco-Betancourt et al. 2004), suggesting a defect in the final stages of B-cell differentiation. A key step in B-cell maturation is isotype switching of immunoglobulins (Ig) through class-switch recombination (CSR). Effective CSR heavily relies on the controlled formation and correct repair of DNA double-strand breaks (DSB) induced by Activation-Induced (Cytidine) Deaminase (AID) at conserved motifs within the switch (S) regions, which are upstream from gene segments that encode distinct constant regions of antibody heavy chains (Alt et al. 2013). Upon break formation, two switch regions are rejoined by non-homologous end-joining (NHEJ), the main cellular pathway to repair DSBs (Alt et al. 2013). This leads to loss of the intervening DNA between the S regions, removal of μ and δ heavy chain constant regions, substitution by a γ, α or ε constant region, and consequently a change in the class of immunoglobulins that is expressed by a B cell.

NHEJ is carried out by the concerted action of the DNA-dependent protein-kinase complex (DNA-PK), comprised of the KU70/KU80 heterodimer and the DNA-PK catalytic subunit (DNA-PKcs), and the downstream effector proteins X-ray repair cross-complementing protein 4 (XRCC4), DNA ligase 4 (LIG4) and non-homologous end-joining factor 1 (NHEJ1) (Alt et al. 2013). In the absence of this classical (c-)NHEJ mechanism, effective CSR is significantly impaired but not absent, as DSB repair is carried out by alternative NHEJ (a-NHEJ). a-NHEJ is a poorly characterized process dependent on poly(ADP-ribose) polymerase 1 (PARP1), X-ray repair cross-complementing protein 1 (XRCC1) and DNA ligase 1 and 3 (LIG1 and LIG3) (Audebert et al. 2004; Paul et al. 2013; Lu et al. 2016).

Mutations in NHEJ genes (e.g. DNA-PKcs and LIG4) are increasingly recognized as the

primary cause of immunodeficiency in patients (Woodbine et al. 2014). Considering the similarities between the immunodeficiency in ICF patients and individuals with defective NHEJ, this raises the question as to whether loss of NHEJ might explain the compromised immune system in ICF patients. Here we demonstrate that ICF2 patient-derived B cells are defective in NHEJ during CSR. Mechanistically, we uncover a regulatory function for ZBTB24 in NHEJ by cooperating with PARP1 and XRCC4/LIG4 during this repair process. This provides a molecular basis for the humoral immunodeficiency in ICF2 patients.

RESULTS

ICF2 patients display features of defective CSR

The immunodeficiency in ICF2 syndrome is characterized by a reduction or even an absence of immunoglobulins (Igs) (hypo- or agammaglobulinemia) and decreased numbers of switched memory B cells, while normal levels of total B cells are observed (de Greef et al. 2011; Weemaes et al. 2013). We corroborated these findings by showing hypogammaglobulinemia in sera of three independent ICF2 patients, but normal serum levels in age-matched controls (Table S1). Moreover, we characterized peripheral blood lymphocytes by immunophenotyping and found a decrease in the number of switched memory B cells, while numbers of total B cells, naive B cells and unswitched memory B cells were unaffected (Fig. 1A). Of note, total numbers of CD4+ T cells, as well as naive, central memory and CD27+CD28+ early antigen experienced CD4+ T cells were increased when compared to age-matched controls, while those for CD8+ T cells were normal (Fig. S1).

These findings could suggest a defect in V(D)J recombination or class-switch recombination (CSR), which are processes that are critical for B-cell development and ultimately define antibody production and diversification. We therefore first examined the combinatorial diversity of VDJ usage and composition of the junctional region during V(D)J recombination by sequencing immunoglobulin heavy chain gene rearrangements in B cells derived from peripheral blood mono-nuclear cells (PBMCs) of the three ICF2 patients. However, the usage of V, D and J gene segments, as well as the composition of the junctional regions, meaning the number of nucleotide deletions and insertions of non-templated nucleotides by terminal deoxynucleotidyl transferase (TdT) (N-nucleotides), in these patients resembled that of controls (Fig. S2). This suggests that ICF2 patients do not suffer from major defects in V(D)J recombination.

To examine CSR defects in these ICF2 patients, we tested whether patient-derived B cells can undergo CSR in vitro, by stimulating PBMCs in cell culture and measuring the production of total IgA and IgG. For all patients analyzed, the capacity to produce IgA and IgG in vitro was significantly impaired compared to healthy controls (Fig. 1B). We then analyzed the relative abundance of IgG subclasses through RNA sequence analysis of IgH transcripts in the patient-derived PBMCs (Fig. 1C). When comparing relative abundance of IgG1-4 to age-matched controls, we observed a decrease in the relative expression of IgG1, accompanied by an increase in relative IgG3 expression in ICF2 patients (Fig. 1D). Together, these data show that the absence or reduction of Igs in combination with changes in the relative abundance of Ig subclasses in ICF2 patients is most likely caused by impaired CSR.

Loss of ZBTB24 resembles NHEJ-deficiency in CSR

CSR heavily relies on the c-NHEJ-mediated repair of AID-induced DSBs upstream of the

constant regions of the IgH locus (Alt et al. 2013). To study the functional consequences of ZBTB24 mutations in the repair of DSBs during CSR, a PCR-based assay for amplification of Sμ-Sα junctions (located upstream of the Cm and Ca regions of the IgH locus, respectively; Fig. 1C) was performed on the ICF2-patient cells. Twelve Sμ-Sα junctions from the patients were then compared to our previously published 183 Sμ-Sα junctions from healthy children controls (Du et al. 2008; Enervald et al. 2013). The junctions from the ICF2-deficient patients showed an altered repair pattern with an increased usage of long (7-9bp) microhomologies (33% vs. 10% in controls, χ 2 test, p=0.035, Table 1), suggesting a shift to the use of an alternative end-joining pathway in the cells from the patients. A similar shift is also apparent in NHEJ-deficient cells from patients with mutations in Artemis or LIG4 (Table 1), suggesting that the shift to alternative repair may be due to a defect in NHEJ. Furthermore, 11 Sμ-Sg junctions (located upstream of the Cm and Cg regions of the IgH locus, respectively; Fig. 1C) were isolated from the ICF2-deficient cells and compared to our previously published 58 Sμ-Sg junctions from healthy children controls (Du et al. 2008). Although the repair pattern at the Sμ-Sg junctions were largely normal (Table 1), one Sμ-Sg junction showed a "footprint"

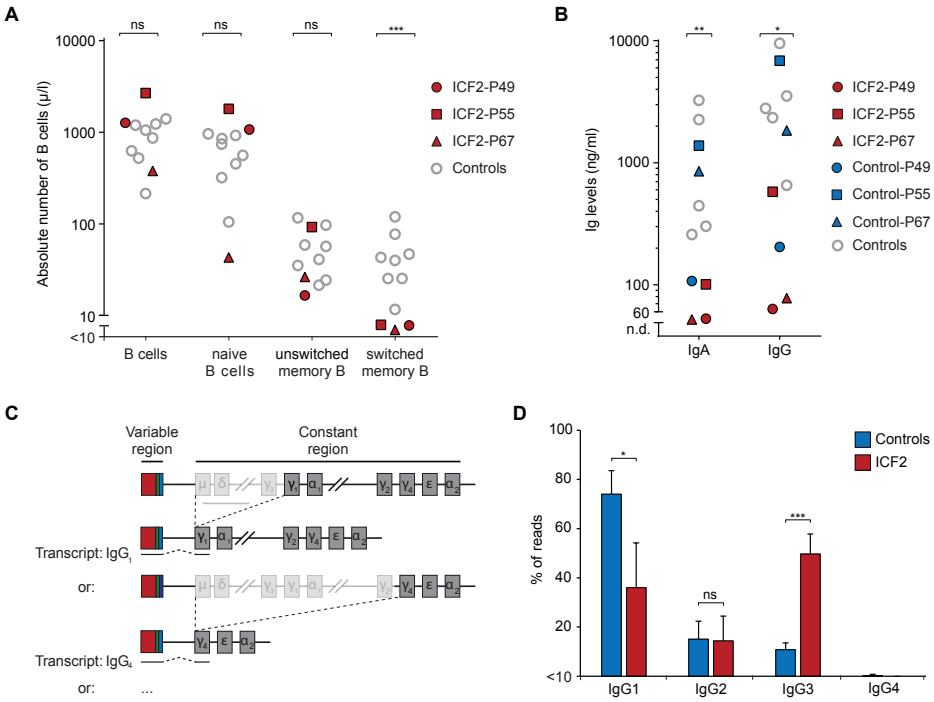

Figure 1. Defective CSR in ICF2 patients due to loss of ZBTB24-dependent NHEJ. (A) Number of cells within the indicated differentiation stages of the total peripheral blood CD19+/CD20+ B-cell population was measured by flow cytometry. Naive B cells: IgMdull, IgD++, CD27-; unswitched memory B cells: IgM++, IgDdull, CD27+; switched memory B cells: IgM-, IgD-, CD27+. Closed red symbols are the ICF2 patients P49, P55 and P67. Open grey circles represent 8 healthy age-matched controls (age range 0.8 to 4.3 years). (B) PBMC were stimulated with aCD40L, aIgM, CpG and IL-21. After 7 days IgG and IgA concentrations were determined by ELISA assays. Respective controls for the ICF patients P49, P55 and P67 (red symbols) are a healthy brother, a father and a mother (blue symbols). Open grey circles represent 5 unrelated adult controls. PBMC of patients at the age of 0.9, 0.8 and 3.6 years were used. n.d.: not detectable. (C) Schematic representation of the IgH locus with a rearranged VDJ exon (variable domain) and the constant regions. Switching to IgG1 and IgG4 is depicted. (D) Frequency of IgG subclass usage with unique switched IGG transcripts in ICF2 patients and controls.

Table 1: Characterization of CSR junctions[a]

Study subjects	Perfectly matched short homology						No. of junctions
	0 bp						
	Direct end-joining	Small insertions	1-3 bp	4-6 bp	7-9 bp	≥ 10 bp	
Sμ-Sα							
ICF2-deficient	1 (8%)	0 (0%)	3 (25%)	3 (25%)	**5 (42%)**↑	0 (0%)	12
Lig4-deficient[b]	1 (3%)	**0 (0%)**↓	7 (23%)	4 (13%)	4 (13%)	**14 (47%)**↑	30
Artemis-deficient[c]	0 (0%)	6 (11%)	10 (19%)	8 (15%)	9 (17%)	**21 (39%)**↑	54
Controls (1-13 years)[d]	31 (17%)	42 (23%)	36 (20%)	29 (16%)	19 (10%)	26 (14%)	183
Sμ-Sγ							
ICF2-deficient	4 (36%)	0 (0%)	7 (64%)	0 (0%)	0 (0%)	0 (0%)	11
Lig4-deficient[b]	4 (12%)	11 (32%)	15 (44%)	4 (12%)	0 (0%)	0 (0%)	34
Artemis-deficient[c]	5 (21%)	4 (17%)	14 (58%)	1 (4%)	0 (0%)	0 (0%)	24
Controls (1-6 years)[e]	13 (22%)	9 (16%)	26 (45%)	10 (17%)	0 (0%)	0 (0%)	58

a. Statistical analysis was performed by χ^2 test and significant changes are indicated in bold. *p<0.05, **p<0.01, ***p<0.001
b. Previously published CSR junctions from Lig4-deficient patients (Pan-Hammarström et al., 2005)
c. Previously published CSR junctions from Artemis-deficient patients (Du et al., 2008)
d. Previously published Sμ-Sα junctions from children controls (Du et al., 2008; Enervald et al., 2013)
e. Previously published Sμ-Sγ junctions from children controls (Du et al., 2008)

of sequential switching (Sm-Sg3-Sg2; 9%), which is rarely observed in controls (2%), but frequently seen in NHEJ-defective cells such as Artemis- or DNA-PKcs-deficient cells (Du et al. 2008; Bjorkman et al. 2015). Thus, the altered CSR patterns in ICF2 patient cells and their resemblance to those observed in several known NHEJ-deficient patients suggest that ZBTB24 might be a novel NHEJ factor involved in CSR.

ZBTB24 promotes DSB repair via classical NHEJ

To assess whether ZBTB24 is involved in NHEJ, which is the dominant pathway for the repair of DSBs in mammalian cells, we made use of the well-established HEK293T EJ5-GFP reporter cell line. This reporter contains a GFP expression cassette in which the promoter is separated from the GFP gene by a puromycin-resistance gene that is flanked by I-SceI recognition sequences. Following expression of I-SceI endonuclease, repair of the ensuing DSBs will occur through NHEJ and restore GFP expression, which can be used as a measure of NHEJ efficiency (Fig. 2A) (Bennardo et al. 2008). Strikingly, depletion of ZBTB24 by different siRNAs resulted in a marked decrease in NHEJ, which was comparable to the impact of depleting XRCC4 (Fig. 2B-C). Cell cycle profiles remained unaffected in these cells, ruling out effects of cell cycle misregulation (Fig. S3A). siRNAs against ZBTB24 not only reduced expression of ZBTB24 mRNA (Fig. 2C), but also that of exogenously expressed GFP-ZBTB24 (Fig. S3B).

The two major known pathways for the end-joining-dependent repair of DSBs in

mammalian cells are c-NHEJ and a-NHEJ (Alt et al. 2013). Although the EJ5 reporter cannot differentiate between these pathways (Bennardo et al. 2008), we observed a remarkably similar phenotype following loss of ZBTB24 or the c-NHEJ factor XRCC4. Moreover, ICF2

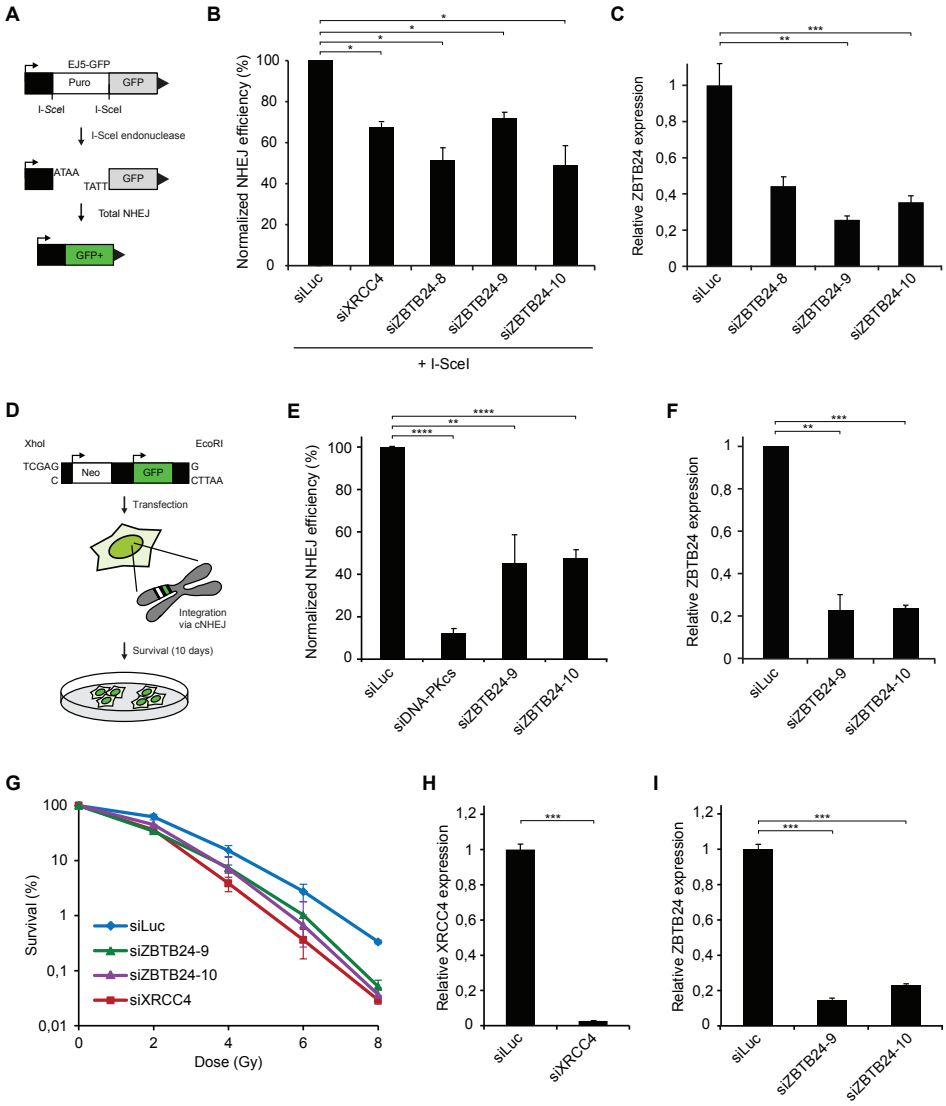

Figure 2. ZBTB24 promotes DSB repair via c-NHEJ. (A) Schematic representation of the EJ5-GFP reporter for NHEJ. (B) HEK293T EJ5-GFP cells were treated with the indicated siRNAs and 48h later co-transfected with I-SceI (pCBASce) and mCherry expression vectors. The ratio of GFP/mCherry expressing cells was counted by flow cytometry 48h later. (C) Cells from B were subjected to RNA extraction. cDNA was synthesized from total RNA samples followed by qPCR to determine the expression levels of ZBTB24. (D) Schematic of the plasmid integration assay. pEGFP-C1 plasmid containing Neo and GFP markers is linearized with the indicated restriction enzymes and transfected into U2OS cells. Stable integrants are selected on medium containing G418. GFP was used as a control for transfection efficiency. (E) Plasmid integration assays in U2OS cells transfected with indicated siRNAs. (F) As in C, except that cells from E were used. (G) VH10-SV40 cells were treated with the indicated siRNAs for 48h, exposed to different doses of IR and scored for clonogenic survival. (H) As in C, except that cells from G were used to monitor XRCC4 expression. (I) As in C, except that cells from G were used.

patient cells showed altered CSR patterns that resembled those observed in patient cells deficient for the c-NHEJ factor LIG4 (Table 1), suggesting a role for ZBTB24 in c-NHEJ. To provide further support for this, we used a plasmid integration assay to specifically study the role of ZBTB24 in c-NHEJ. In this assay, a linearized plasmid encoding GFP and a Neomycin-selection marker is transfected into U2OS cells. Survival of G418-resistant colonies relies on the genomic integration of the linear plasmid via c-NHEJ (Fig. 2D). Depletion of DNA-PKcs (catalytic subunit of DNA-PK complex) resulted in an 80-90% decrease in cell survival, indicating the assay provides a read-out for c-NHEJ (Fig. 2E and S3C). Moreover, knockdown of ZBTB24 caused a ~50% reduction in c-NHEJ efficiency when compared to control cells (Fig. 2E-F and S3D).

To rule out that ZBTB24 regulates NHEJ indirectly through transcriptional regulation of DSB repair factors, we depleted ZBTB24 and performed whole transcriptome analysis using RNA sequencing in HEK293T cells. In total we found 158 differentially expressed genes (FDR < 0.05), of which 90 are upregulated and 68 are downregulated (Table S2). We compared the list of deregulated genes with 66 unique genes in GO-term 0006302 (DSB repair), but did not find any overlapping genes (Fig. S4). This strongly suggests that ZBTB24 does not affect NHEJ through transcription regulation of DSB repair genes.

To assess the functional relevance of ZBTB24 in NHEJ, we investigated its ability to protect cells against DNA breaks induced by ionizing radiation (IR). To this end, clonogenic survival of VH10-SV40 cells depleted for ZBTB24 or XRCC4 was determined after exposure to IR. This showed a similar dose-dependent decrease in the survival capacity of ZBTB24-depleted and XRCC4-depleted cells when compared to control cells (siLuc; Fig. 2G-I). Collectively, these results underpin the functional importance of ZBTB24 in the protection of cells against DNA breaks and implicate a role for ZBTB24 in DSB repair by NHEJ.

ZBTB24 interacts with PARP1 in a PARylation-dependent manner

To assess how ZBTB24 affects NHEJ, we aimed to identify its interaction partners using an unbiased, quantitative proteomics approach. We expressed GFP-ZBTB24 or GFP (control) in U2OS cells and performed GFP-trap-based immunoprecipitation (IP) followed by mass spectrometry (MS) after stable isotope labelling of amino acids in culture (SILAC) (Fig. 3A). Our screen identified 110 proteins that were at least four-fold enriched over control cells (Table S3). Interestingly, besides all core histones, poly(ADP-ribose) polymerase 1 (PARP1), an enzyme implicated in DNA repair, was among the potential interactors of ZBTB24 (Fig. 3A and Table S3). To explore this further, we performed the reciprocal experiment using cells expressing GFP-PARP1. This screen identified 21 proteins that were at least two-fold enriched over control cells (Table S4). Remarkably, not only did we find several known PARP1-interactors such as XRCC1, LIG3 and DNA polymerase beta (POLB) (Pines et al. 2013), also ZBTB24 was among the top hits of this screen (Fig. 3B and Table S4). To confirm the ZBTB24-PARP1 interactions, we performed co-immunoprecipitation (co-IP) experiments followed by western blot analysis. PARP1, as well as histone H3, were detected in the IP fraction of GFP-ZBTB24, whereas in the reciprocal co-IP GFP-PARP1 efficiently precipitated Myc-ZBTB24 (Fig. 3C and S5A). Control co-IP experiments using GFP-NLS expressing cells did not reveal interactions between GFP and either PARP1, H3 or Myc-ZBTB24 (Fig. 3C and S5A). We were unable to demonstrate an interaction between PARP1 and endogenous ZBTB24, because all available antibodies failed to detect ZBTB24 on western blots (data not shown). PARP1 can attach negatively charged ADP-ribose units to itself or other target proteins, forming poly(ADP)-ribose (PAR) chains through a process known as PARylation (Pines et al.

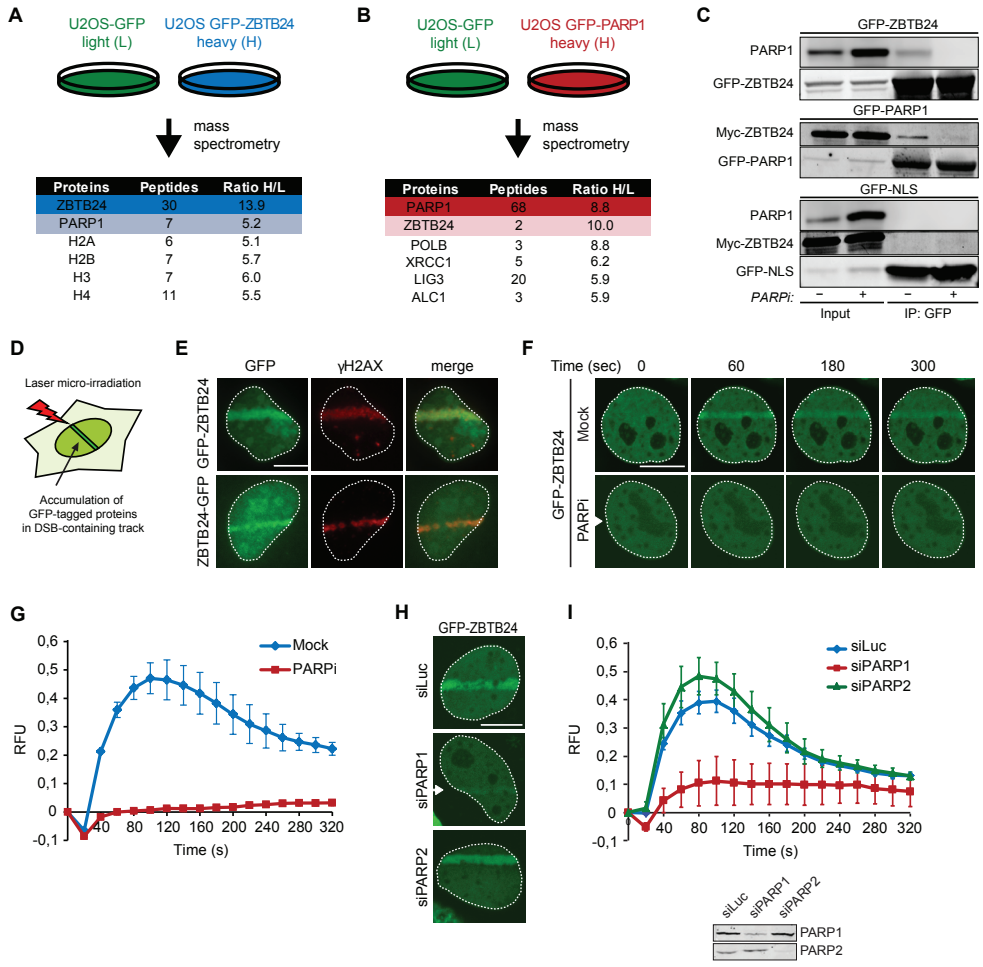

Figure 3. PARP1 interacts with ZBTB24 in a PARylation-dependent manner and recruits ZBTB24 to sites of DNA damage. (A) Schematic representation of SILAC-based mass spectrometry (MS) approach. GFP- or GFP-ZBTB24 expressing U2OS cells were labelled with Lys0 and Arg0 (L) or Lys8 and Arg10 (H), respectively. Lysates were subjected to GFP-Immunoprecipitation (IP) and equal amounts of both IP fractions were mixed. Proteins in the IP fractions were digested by trypsin and subjected to MS analysis. A list of ZBTB24-interacting proteins, including the number of peptides and the interaction ratio from heavy (H)- over light (L)-labelled cell extracts as revealed by MS, is shown. (B) As in A, but with GFP- and GFP-PARP1 expressing U2OS cells. (C) Cells expressing GFP-ZBTB24, GFP-PARP1 and Myc-ZBTB24, or GFP-NLS and Myc-ZBTB24 were either treated with DMSO (Mock) or with PARP inhibitor (PARPi). Whole cell extracts (WCEs) were subjected to GFP-IP followed by western blot analysis of the indicated proteins. (D) Schematic representation of the laser micro-irradiation approach. (E) GFP-ZBTB24 or ZBTB24-GFP accumulate at γH2AX-decorated DNA damage tracks following transient expression and laser micro-irradiation in U2OS cells. (F) As in E, except that transiently expressing GFP-ZBTB24 cells were either treated with DMSO (Mock) or PARPi before GFP-ZBTB24 accumulation was monitored at the indicated time points after laser micro-irradiation. (G) Quantification of the results from F. RFU is Relative Fluorescent Units. (H) As in F, expect that cells were co-transfected with GFP-ZBTB24 and the indicated siRNAs. (I) Quantification of the results from H (upper panel). Western blot showing the knockdown efficiency of PARP1 and PARP2 (bottom). Scale bar 10 µm.

2013). Upon addition of PARP inhibitor (PARPi), PARylation was efficiently inhibited and the interaction between ZBTB24 and PARP1 was lost (Fig. 3C and S5B). Together, these results suggest that ZBTB24 and PARP1 interact in a PARylation-dependent manner.

PARP1 recruits ZBTB24 to sites of DNA damage

PARP1 binds to both single- and double-strand breaks, where it promotes the assembly of chromatin remodelers and DNA repair proteins (Pines et al. 2013). Given the interaction between ZBTB24 and PARP1, we tested whether ZBTB24 is recruited to sites of DNA damage. We found that both N- and C-terminally tagged ZBTB24 localize at laser micro-irradiation-induced tracks containing γH2AX, a known marker of DNA damage (Fig. 3D-E). Importantly, ZBTB24 recruitment to such DNA damage tracks was completely abrogated upon treatment with PARPi (Fig. 3F-G), demonstrating its dependency on PARylation. Furthermore, the accumulation of ZBTB24 at DNA damage tracks was rapid but transient, reaching maximum levels at ~100 seconds after DNA damage induction (Fig. 3G) and resembling much the reported dynamics of PARP1 accrual and PARylation at sites of DNA damage (Mortusewicz et al. 2007). Importantly, siRNA-mediated depletion of PARP1, but not PARP2, abrogated ZBTB24 accumulation in laser tracks (Fig. 3H-I). These results show that ZBTB24 is rapidly recruited to sites of DNA damage in a PARP1- and PARylation dependent manner.

PAR chains are rapidly hydrolysed by the activity of poly(ADP-ribose) glycohydrolase (PARG), which explains the rapid turn-over of PAR chains at sites of DNA damage (Pines et al., 2013). To prevent this rapid turnover, we increased the steady-state levels of PAR chains by siRNA-mediated depletion of PARG (Fig. S6A). Under these conditions, we observed enhanced and more persistent accumulation of ZBTB24 at sites of damage (Fig. S6B-C). In contrast, overexpression of mCherry-tagged PARG resulted in a dramatic decrease in the total level of PARylation and abrogated recruitment of ZBTB24 to sites of damage (Fig. S6D-F), phenocopying the effect observed after loss of PARP1 activity (Fig. 3F-G). Thus, the PARP1- and PARG-dependent turnover of PAR chains at DNA lesions is a critical determinant of the rapid and transient accumulation of ZBTB24.

The ZNF of ZBTB24 binds PAR to promote PARP1-dependent ZBTB24 recruitment

Three conserved domains can be identified in ZBTB24: an N-terminal BTB domain (amino acids 9-132), a small AT-hook DNA-binding domain (amino acids 159-171) and 8 tandem C2H2 zinc-finger (ZNF) motifs (amino acids 294-512) (Fig. 4A). To dissect the relevance of these domains for ZBTB24's interaction with PARP1 and localization to DNA damage, we generated and expressed GFP-fusion constructs of the different domains (Fig. 4B-E). Interestingly, GFP-BTB, GFP-BTB-AT or GFP-ΔZNF did not accumulate at sites of laser-induced DNA damage, whereas GFP-BTB-AT-ZNF (GFP-BAZ) and GFP-ZNF were recruited with similar kinetics as GFP-ZBTB24 (Fig. 4C and S7). Moreover, similar to GFP-ZBTB24 (Fig. 3F-G), GFP-BAZ and GFP-ZNF accumulation was abolished upon PARP inhibition (Fig. S7). This suggests that the ZNF domain is essential for the PARP1 activity-dependent accumulation of ZBTB24 at sites of DNA damage.

PARP1 is responsible for ~85% of the synthesized PAR chains and attaches these moieties to itself and other proteins (Shieh et al. 1998; Mortusewicz et al. 2007). The PAR-dependent accumulation of ZBTB24 could be a consequence of the PARylation of ZBTB24 by PARP1 or could be due to the capacity of ZBTB24 to bind PARP1-associated PAR chains. To examine whether ZBTB24 itself is PARylated, we exposed cells to IR or the DNA-alkylating agent N-methyl-N'-nitro-N-nitrosoguanidine (MNNG) and compared the PARylation status of ZBTB24 to that of PARP1. We observed a significant increase in PARylated proteins after MNNG treatment, and a modest increase shortly after exposure to IR (Fig. S8A), indicating that these treatments result in activation of PARP enzymes. We subsequently immunoprecipitated GFP-ZBTB24 or GFP-PARP1 from these cells using stringent, high-salt wash conditions to disrupt all non-

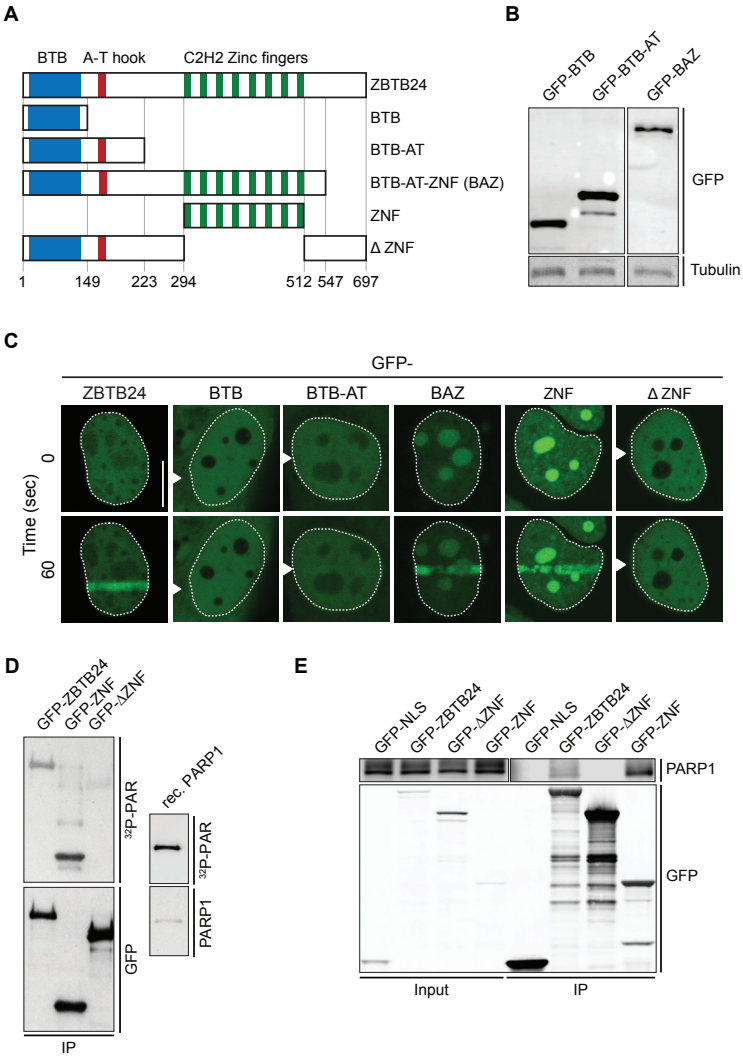

Figure 4. The ZNF domain in ZBTB24 interacts with PAR and mediates its recruitment to sites of DNA damage. (A) Schematic representation of isoform 1 of ZBTB24 and its BTB-, DNA-binding AT hook- and 8 x C2H2 zinc finger domain. Protein domains were separated as indicated and fused to GFP for functional analysis. (B) Western blot analysis of WCEs from U2OS cells expressing the indicated GFP-tagged ZBTB24 domains. (C) Accumulation of the indicated GFP-tagged ZBTB24 domain in laser micro-irradiated U2OS cells. Representative images of unirradiated and irradiated cells (taken at the indicated time point after irradiation) are shown. Scale bar 10 µm. (D) HEK293T cells expressing the indicated GFP-tagged ZBTB24 domains were subjected to GFP-IP followed by western blot analysis and membrane-exposure to radioactive PAR (32P-PAR). Recombinant (rec.) PARP1 is a positive control. (E) Lysates from U2OS cells transiently expressing either GFP-NLS or the indicated GFP-tagged ZBTB24 domains were subjected to GFP-IP and western blot analysis for the indicated proteins.

covalent protein-protein interactions, and examined their PARylation status by western blot analysis. As expected, PARP1 was strongly PARylated under all conditions (Fig. S8B), showing that our approach can detect the attachment of PAR chains to proteins. However, we failed to detect PARylation of ZBTB24 under these conditions, suggesting that ZBTB24 is not a preferred target for PARylation by PARP1 (Fig. S8B).

Next, we examined if ZBTB24 could physically associate with PAR chains in vitro by using southwestern blotting. GFP-ZBTB24 was immunoprecipitated, transferred to a membrane and exposed to in vitro generated 32P-labelled PAR chains. Indeed, GFP-ZBTB24, similar to recombinant PARP1, was able to bind PAR chains efficiently (Fig. 4D). Since the ZNF domain in ZBTB24 is a key determinant of the PARP1 activity-dependent recruitment of ZBTB24 to sites of DNA damage, we examined if this domain would mediate the interaction with PAR polymers. We observed that GFP-ZNF, but not GFP-ΔZNF (full-length ZBTB24 lacking the ZNF domain), could bind to PAR chains (Fig. 4D). In concordance, co-IP experiments revealed an interaction between PARP1 and GFP-ZNF, but not GFP-ΔZNF (Fig. 4E). Together these results suggest that the ZNF of ZBTB24 is a novel PAR-binding domain that mediates ZBTB24 recruitment to DNA damage through interactions with PARylated PARP1.

ZBTB24 promotes PAR synthesis and protects PAR chains

Considering that ZBTB24 efficiently associates with PARP1-generated PAR chains, we wondered whether ZBTB24 could be involved in regulating the steady-state levels of such chains in response to DNA damage. To examine this possibility, we monitored global PAR levels by western blot analysis in cells exposed to IR. While hardly any PARylation could be observed in mock-treated cells, exposure to IR triggered robust DNA damage-induced PARylation (Fig. 5A-B), which was largely suppressed (~60-70%) by knockdown of PARP1 (Fig. 5A-B). Strikingly, knockdown of ZBTB24 also caused a significant reduction (~50%) in PARylation in IR-exposed cells (Fig. 5A-B), suggesting that ZBTB24 is required to boost the DNA damage-induced PARylation response.

It is feasible that ZBTB24 regulates steady-state PAR levels by either stimulating the synthesis of such chains, or by preventing their degradation. To examine a potential stimulatory role for ZBTB24 in PAR synthesis, we reconstituted PARP1-dependent synthesis of PAR in an in vitro system in the absence or presence of recombinant ZBTB24 (Fig. 5C). In the presence of NAD+ and a damaged DNA template, we found that the capacity of recombinant PARP1 to synthesize PAR chains was enhanced in a dose-dependent manner by the presence of recombinant ZBTB24 (Fig. 5D-E), suggesting that ZBTB24 stimulates PARP1-dependent PAR synthesis.

Another non-mutually exclusive possibility is that ZBTB24 binding to PAR chains protects such chains from efficient hydrolysis by the PARP1 antagonist PARG (Fig. 5D). To explore this possibility, we allowed PARP1-dependent synthesis of PAR in our in vitro system and, following the inactivation of PARP1 by PARPi, added recombinant PARG hydrolase with increasing amounts of recombinant ZBTB24 (Fig. 5F). We could detect efficient hydrolysis of nearly all PAR chains in the absence of ZBTB24 (lane 1 versus 2; Fig. 5G). Interestingly, ZBT24 inhibited in a dose-dependent manner the break-down of PAR products in the hydrolysis reaction (Fig. 5G-H), suggesting that ZBTB24 can protect PAR chains from PARG-dependent degradation. In conclusion, we found that ZBTB24 promotes the steady-state levels of DNA damage-induced PAR chains by simultaneously stimulating the PARP1-dependent synthesis and inhibiting the PARG-dependent hydrolysis of such chains.

ZBTB24 and PARP1 promote c-NHEJ by regulating XRCC4/LIG4 assembly

We then sought to address how ZBTB24's role in PAR synthesis and protection is linked to its involvement in c-NHEJ (Fig. 2). It is known that c-NHEJ involves the binding of KU70/KU80 to the broken ends, followed by the accrual of DNA-PKcs and ligation of the break by the XRCC4/DNA ligase 4 (LIG4) complex (Alt et al. 2013). Interestingly, recent in vitro studies

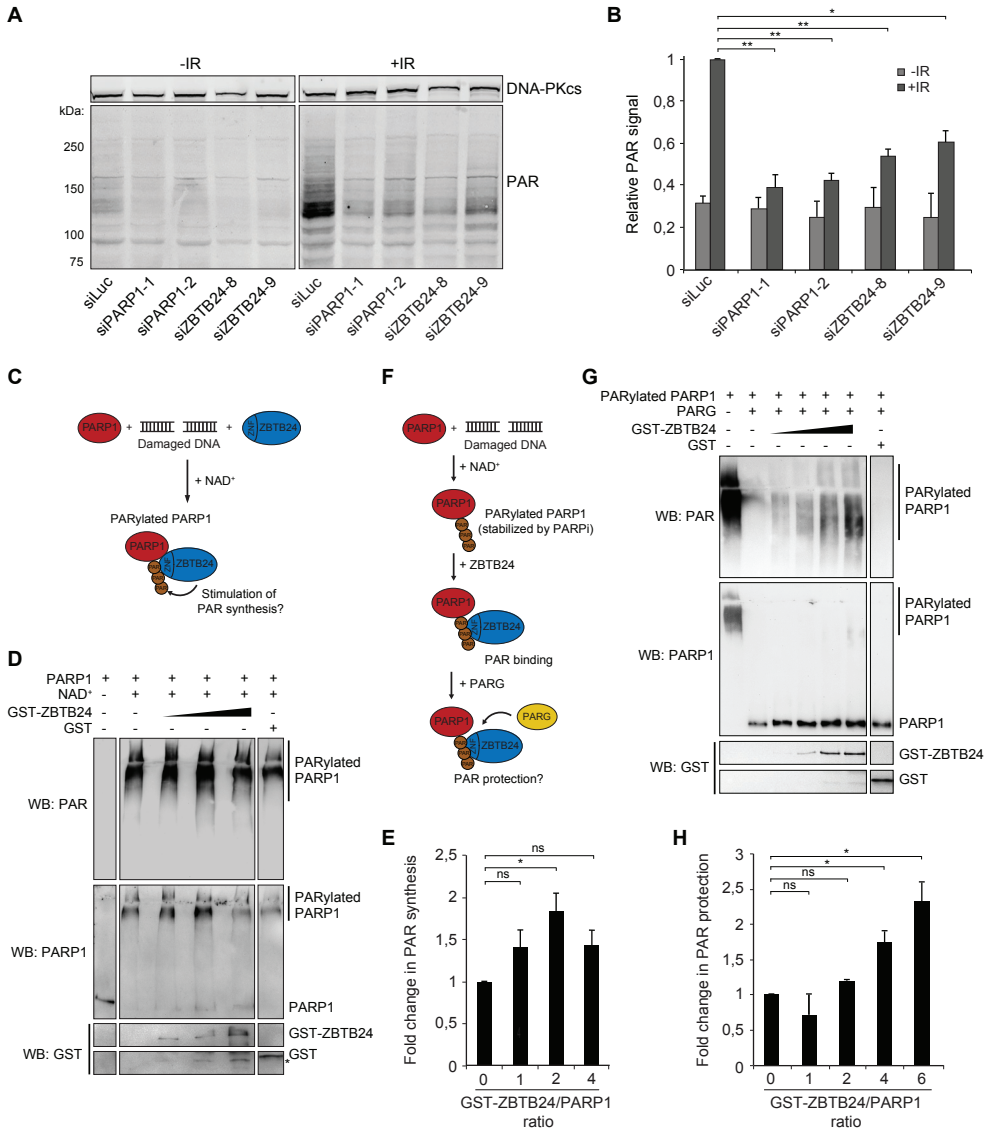

Figure 5. ZBTB24 stimulates PARP1-dependent PAR synthesis and protects PAR chain stability. (A) U2OS cells transfected with the indicated siRNAs were left untreated or exposed to IR. Five minutes later WCE were prepared and subjected to western blot analysis for DNA-PKcs and PAR. DNA-PKcs is a loading control. (B) Quantification of the results from A and a second independent experiment. The ratio of PAR/loading control signals per sample was normalised to that of the IR-exposed siLuc sample, which was set to 1. (C) Schematic of the PAR synthesis assay. (D) Recombinant PARP1 was incubated with a damaged DNA template and activated by NAD+ in the presence of increasing concentrations of GST-ZBTB24 or GST only. The presence of 10H-PAR chains and recombinant proteins was monitored by western blot analysis. (E) Quantification of ZBTB24-dependent stimulation of PAR synthesis from D and two other independent experiments. The signal of 10H-PAR for each sample containing GST-ZBTB24 was normalized to that without GST-ZBTB24, which was set to 1. (F) Schematic of the PAR protection assay. (G) Recombinant PARP1 was incubated with a damaged DNA template and activated by NAD+ to generate PARylated PARP1. Increasing concentrations of GST-ZBTB24 or GST alone were added, followed by incubation wit PARG. The presence of 10H-PAR chains and recombinant proteins was monitored by western blot analysis. (H) As in E, except that PAR protection was measured from G and another independent experiment.

demonstrated that the c-NHEJ ligase LIG4 interacts with PAR chains through its C-terminal BRCT domain (Li et al. 2013), providing a possible link between ZBTB24's involvement in PAR stability and NHEJ. To study this further, we first applied laser micro-irradiation to monitor the recruitment of GFP-XRCC4 to damaged DNA in U2OS cells that were either treated with PARP inhibitor or depleted for PARP1. Strikingly, the loss of both PARP activity and PARP1 protein markedly impaired the recruitment of GFP-XRCC4 (Fig. 6A-D), suggesting that PARP1-dependent PARylation regulates the assembly of XRCC4/LIG4 complexes at sites of DNA damage to promote c-NHEJ. To investigate this, we used the plasmid integration assay to specifically examine PARP1's contribution to c-NHEJ. In agreement with our recruitment data, we found that PARP1 depletion resulted in a ~40% reduction in c-NHEJ efficiency (Fig. 6E and S3C), suggesting that PARP1, similar to ZBTB24 (Fig. 2E), plays a role in c-NHEJ.
Given ZBTB24's role in NHEJ, its interaction with PARP1 and its stimulatory effect on PARylation, we addressed whether it affects the PARP1-dependent assembly of XRCC4/LIG4 at DSBs. Depletion of ZBTB24, similar to that of PARP1, resulted in a strong reduction in GFP-XRCC4 recruitment at sites of laser-induced DNA damage (Fig. 6F-G). Moreover, ZBTB24 depletion also reduced the accumulation of endogenous XRCC4, while DNA damage levels measured by γH2AX formation were comparable to that of control cells (Fig. S9). Importantly, the accumulation of GFP-XRCC4 at a stably integrated Lactose operator (LacO) array upon tethering of a Lactose repressor (LacR)-tagged FokI nuclease in U2OS cells was also strongly reduced in cells depleted for ZBTB24 (Fig. 6H-K). This indicates that ZBTB24 acts at bona fide DSBs to facilitate the accumulation of functional XRCC4/LIG4 complexes. Together our results show that ZBTB24, by ensuring robust steady-state levels of DNA damage-induced PARylation, acts as a scaffold for the PARP1 - LIG4 interaction to promote XRCC4/LIG4-dependent c-NHEJ (Fig. 6L).

DISCUSSION

Mutations in at least four different genes cause the primary immunodeficiency ICF. About 30% of the ICF patients carry causal mutations in the uncharacterized ZBTB24 gene (ICF2) (Weemaes et al. 2013; Thijssen et al. 2015). Here, we functionally characterized the role of ZBTB24 by biochemical, cell biological and patient-based approaches. In ICF2 patients, we report a severe reduction in immunoglobulin production and diversification capacity, and a shift towards a-NHEJ events during CSR, which is reminiscent of the phenotype observed in c-NHEJ-deficient patients (Pan-Hammarstrom et al. 2005; Du et al. 2008). These findings provide a plausible molecular explanation for the currently unexplained immunodeficiency in ICF2 and suggest a role for ZBTB24 in c-NHEJ. Indeed, we reveal that ZBTB24 is recruited to sites of DNA damage in a PARP1-dependent manner by associating with PARP1-generated PAR-chains through its ZNF domain. Our biochemical and cellular analyses show that ZBTB24 promotes PARP1-mediated PAR synthesis and acts as a scaffold protein that protects PAR chains from degradation, thereby enhancing the PARP1-dependent recruitment of the LIG4-XRCC4 complex to facilitate efficient DSB repair by c-NHEJ (see model; Fig. 6L).

ZBTB24 is required for CSR, a process defective in ICF2 patients

Mutations in ZBTB24 lead to defective CSR in ICF2 patients, while V(D)J recombination remains unaffected. This may be unexpected considering that both processes heavily rely on c-NHEJ. However, mutations in several other DNA damage response (DDR) genes, such

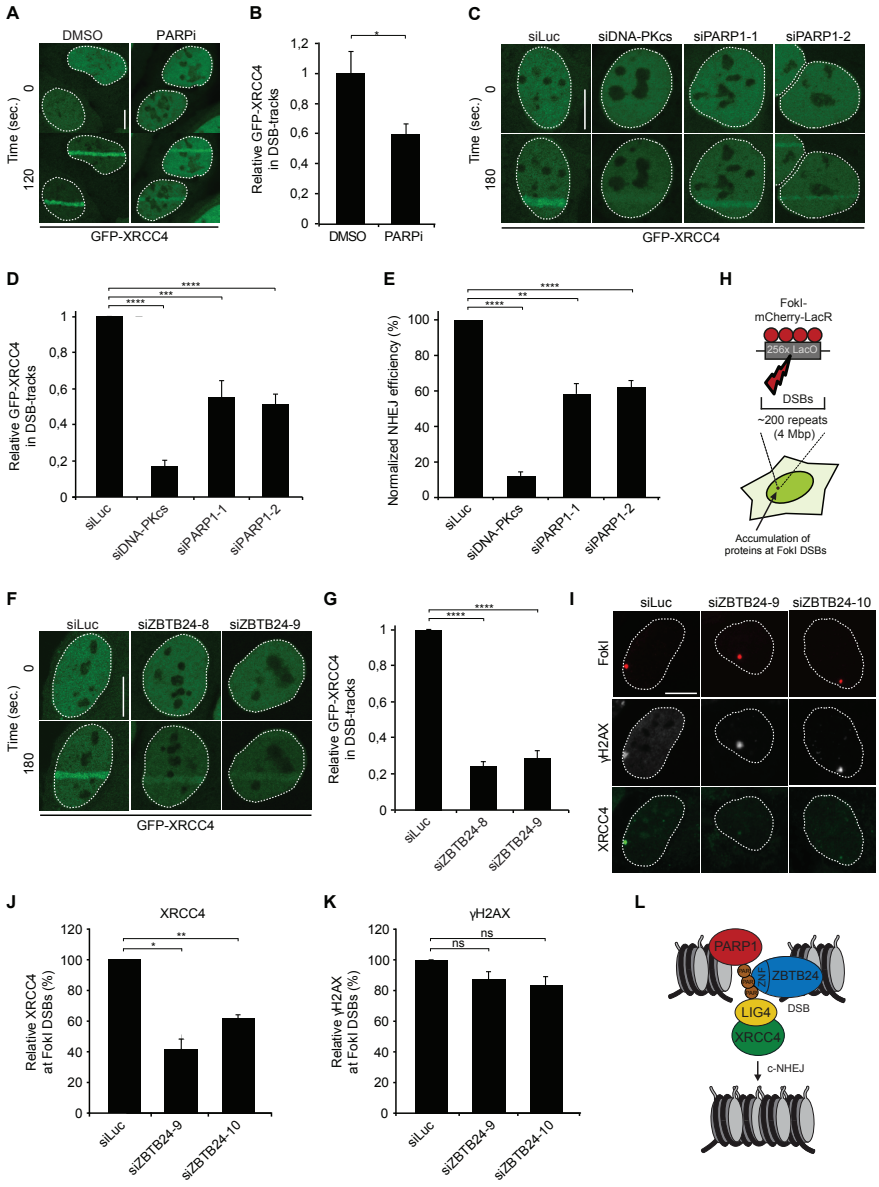

Figure 6. ZBTB24 and PARP1 promote XRCC4/LIG4 assembly at DNA damage sites. (A) U2OS stably expressing GFP-XRCC4 were treated with DMSO (Mock) or PARPi and subjected to laser micro-irradiation. Representative images of unirradiated and irradiated cells (taken at the indicated time point after irradiation) are shown. Arrowheads indicate laser-irradiated regions. Scale bar 10 µm. (B) Quantification of A. (C) As in A, except that cells were transfected with the indicated siRNAs. (D) Quantification of C. (E) Plasmid integration assays in U2OS cells transfected with indicated siRNAs. (F) As in C. (G) Quantification of F. (H) Schematic of the system in U2OS 2-6-3 cells used to locally induce multiple DSBs upon tethering of the FokI endonuclease. (I) Accumulation of XRCC4 (green) to γH2AX-marked (white) DSBs induced by FokI-mCherry-LacR at a LacO array (red) in cells transfected with the indicated siRNAs. Scale bar 10 µm. (J) Quantification of XRCC4 accumulation in F. (K) As in J, except for γH2AX. (L) Model for the role of ZBTB24 in DSB repair by NHEJ. ZBTB24 accumulates at DSBs, where it functions as a scaffold to protect PARP1-associated PAR-chains, which serve as a docking site for the LIG4-XRCC4 complex, facilitating efficient DSB repair via c-NHEJ.

as H2AX, NIPBL and ATM in both mice and humans, cause a remarkably similar defect in CSR without affecting V(D)J recombination (Pan et al. 2002; Reina-San-Martin et al. 2003; Manis et al. 2004; Enervald et al. 2013). It has been suggested that the ends of RAG1/2-induced DSB are held together by these enzymes during V(D)J recombination. In contrast, AID-initiated DSBs during CSR are likely held together by factors involved in the signalling of DSB, such as the core chromatin component H2AX and 53BP1 (Petersen et al. 2001; Manis et al. 2004). The role of ZBTB24 may resemble that of the latter DDR components, explaining its specific impact on CSR. Alternatively, RAG1/2 induce DSBs that are characterized by the production of a hairpin structure at the broken ends. PARP1 swiftly binds to single- and double-strand breaks (Eustermann et al. 2011; Langelier et al. 2012), as well as to hairpin structures in vitro (Lonskaya et al. 2005). However, whether it also displays affinity for RAG1/2-induced hairpin structures at DSBs in vivo remains to be determined. It is conceivable that these structures are not bound by PARP1 due to their processing by the structure-specific endonuclease Artemis (Alt et al. 2013), which could rule out a function for PARP1 and most likely ZBTB24 in V(D)J recombination and would be in agreement with our observations. However, PARP1 seems to have affinity for AID-induced breaks in mice, where it promotes CSR through a-NHEJ (Robert et al. 2009). Whether it also modulates CSR in humans remains elusive, mainly because patients with loss-of-function mutations in PARP1 have not been reported yet.

ZBTB24 and PARP1 in NHEJ

The current models for NHEJ distinguish a dominant c-NHEJ pathway that is fully dependent on KU70/KU80 from a PARP1-dependent a-NHEJ pathway that only becomes active in the absence of KU70/KU80 (Wang et al. 2006). However, while PARP1 is required for a-NHEJ, this does not exclude a stimulatory role for PARP1 in c-NHEJ. Indeed, several studies reported that the loss of PARP1 activity modulates the c-NHEJ-dependent re-joining of DSBs in hamster, mouse and human cells (Veuger et al. 2003; Mitchell et al. 2009). Our results corroborate and extend these observations and further support a role for PARP1 in DSB repair through c-NHEJ.

Our work identifies ZBTB24 as an effector of PARP1-dependent c-NHEJ. However, the c-NHEJ-specific phenotypes, such as impaired random plasmid integration or XRCC4 recruitment to laser/nuclease-induced DSBs, which we observed after knockdown of ZBTB24 or PARP1, were not as strong as seen after depletion of core NHEJ factors, such as DNA-PKcs. This suggests that the PARP1-ZBTB24 axis is not essential for c-NHEJ, but greatly stimulates this process in human cells.

Loss of ZBTB24 also reduces NHEJ in the EJ5-GFP reporter. Since this reporter cannot discriminate between c-NHEJ and a-NHEJ, we cannot rule out the possibility that ZBTB24 might promote both c-NHEJ and a-NHEJ. An involvement in the latter repair pathway would not be surprising given its interaction with PARP1, which is required for a-NHEJ (Pines et al. 2013).

The C2H2 ZNF of ZBTB24 binds PAR chains

Four structurally distinct protein motifs have been characterized to mediate interactions with PAR chains: 1) a consensus of eighth interspersed basic and hydrophobic amino acid residues, 2) macro domains containing a conserved ligand-binding pocket, 3) the WWE domain that recognizes iso-ADP-ribose, which is the smallest internal structural unit of PAR, and 4) the PAR-binding zinc (PBZ) finger (Kalisch et al. 2012). Here we expand the latter

category by showing that the C2H2 ZNF, as present in ZBTB24, is a new type of motif that mediates PAR binding. While this motif has been suggested to predominantly bind to DNA (Najafabadi et al. 2015), we demonstrate that the eight C2H2 ZNFs within ZBTB24 associate with PAR chains in vitro and mediate the interaction with PARP1 in in vivo. Interestingly, a recent screen for DDR factors identified more than 100 new proteins, many of which were ZNF-containing transcription factors that, similar to ZBTB24, were recruited to sites of laser-induced DNA damage in a PARP/PARylation-dependent manner (Izhar et al. 2015). Further studies on these DNA damage-associated ZNF-containing proteins may reveal, whether they have evolved as general PAR-binding proteins with specialized functions in the PARP-dependent DDRs.

ZBTB24 stimulates PAR synthesis and protects PAR chains

Based on its functional domains ZBTB24 seems to lack enzymatic activity. Indeed, our work suggests that ZBTB24 has at least two non-catalytic roles: it can enhance PAR synthesis by PARP1 and can bind and protect PAR chains from hydrolysis by PARG. How does ZBTB24 stimulate PAR synthesis by PARP1? Two models exist for the activation of human PARP1: the cis and trans model. In the cis model a single PARP1 protein binds a DNA end, which triggers intramolecular interactions and conformational changes that enhance the flexibility of the catalytic domain to induce auto-PARylation (Langelier et al. 2012). One possibility is that ZBTB24 by binding to PARP1 stimulates these intramolecular interactions and conformational changes, resulting in enhanced PARP1 activation. Alternatively, in the trans model, two PARP1 proteins dimerize at a DSB, subsequently enabling one of these PARP1 molecules to modify the catalytic domain of its interaction partner (Ali et al. 2012). BTB domains, such as those found in ZBTB24, are known to mediate dimerization between proteins (Bardwell and Treisman 1994). It is therefore possible that ZBTB24's interaction with PARP1 and its ability to dimerize could stimulate PARP1 dimerization and its subsequent activation. Additional biochemical work will be required to reveal whether ZBTB24 promotes in cis and/or in trans activation of PARP1.

In contrast to ZBTB24's role in PARP1 activation, its contribution to PAR protection may be easier to explain. We demonstrated that ZBTB24 through its ZNF domain directly associates with PARP1-associated PAR chains. This may sterically hinder PARG from attacking PAR chains. However, some PAR chains are digested despite the presence of excess ZBTB24 (Fig. 5G-H), which could be due to the highly versatile endo- and exoglycosidic activities of PARG towards PAR (Brochu et al. 1994). It may be that additional PAR-binding factors are required to provide full protection against PARG hydrolysis. These factors may for instance include one or more ZNF-containing transcription factors or DDR proteins with intrinsically disordered domains that are recruited to sites of DNA damage in a PAR-dependent manner (Altmeyer et al. 2015; Izhar et al. 2015).

We observed that at concentrations up to two times that of PARP1, ZBTB24 can only activate PARP1, while at more than two times the concentration of PARP1 it protects PAR chains rather than that it helps to activate PARP1 (Fig. 5D-E and 5G-H). This suggests that ZBTB24 may switch function dependent on its concentration relative to PARP1. Based on this, at sites of DNA damage we envision a scenario in which ZBTB24, following its initial recruitment, helps with the activation of PARP1 and subsequently protects the synthesized PARP1-associated PAR chains. As such it could facilitate the PARylation-dependent interaction between the c-NHEJ ligase LIG4 and PARP1 (Li et al. 2013), and promote DSB repair by c-NHEJ (Fig. 6L).

MATERIALS AND METHODS

Patients
Sera and PBMC were obtained after informed consent from two ICF2 patients that have been described previously (patients 49 and 55;(Weemaes et al. 2013)) and one novel ICF2 patient (p67) carrying the same recessive mutation as patient 49.

Lymphocyte phenotyping and Ig production analysis
PBMC from patients and healthy individuals were stained with fluorochrome-labelled antibodies against cell surface antigens. Stimulated PBMC were analyzed for IgG and IgA production by sandwich ELISA (see Supplemental Material).

IgH repertoire analysis and switch recombination junctions sequencing
IGH rearrangements and Cα and Cγ transcripts were amplified from PBMC by multiplex PCR (Ijspeert et al. 2014). Purified PCR products were sequenced on 454 GS junior instrument (Roche) according to the manufacturer's recommendations and data analysis was performed using the IGGalaxy tool (Moorhouse et al. 2014). Sμ-Sα and Sμ-Sγ fragments were amplified, cloned and sequenced as described (Pan-Hammarstrom et al. 2005). Repair pattern analysis of CSR junctions was done according to guidelines (Stavnezer et al. 2010).

Cell lines, chemicals, plasmids and transfections
Human cells (see Supplemental Material) were cultured in DMEM, supplemented with antibiotics and 10% fetal calf serum. PARP inhibitor (KU-0058948) was used at a concentration of 10 μM. All indicated ZBTB24 constructs were generated by PCR and general cloning procedures. Plasmid DNA or siRNAs were transfected using JetPEI (Polyplus Transfection), Lipofectamine 2000 or RNAiMAX (Invitrogen) according to the manufacturer's instructions.

DSB repair assays
EJ5-GFP reporter assays were carried out as described previously (Helfricht et al. 2013). Gel-purified XhoI-EcoRI-linearized pEGFP-C1 plasmid was transfected into siRNA-depleted cells to measure random plasmid integration events (see Supplemental Material).

Immunoprecipitation for mass spectrometry and PAR-binding assay
GFP-tagged ZBTB24 and PARP1 were immunoprecipitated, trypsinized, desalted and analyzed on a Q-Exactive Orbitrap mass spectrometer (Thermo Scientific, Germany) coupled to an EASY-nanoLC 1000 system (Proxeon, Odense, Denmark). GFP-ZBTB24 and derivatives were immunoprecipitated, separated by SDS-PAGE and incubated with radioactive PAR. Radioactivity was detected by a phosphor-imager screen.

PARP1 activation and PAR protection
PARP1 activation and PAR protection assays were done as described (Shah et al. 2011), using purified GST or GST-ZBTB24 proteins (see Supplemental Material).

Laser micro-irradiation and FokI assays
Laser micro-irradiation was performed by UV-A micro-irradiation of BrdU-sensitized cells or by multi-photon (MP) irradiation using a titanium-sapphire laser were done as described (Helfricht et al., 2013). U2OS 2-6-3 cells expressing inducible FokI-mCherry-LacR were

treated with 300 nM 4-OHT and 1 µM Shield-I for 5 hrs (Shah et al. 2011). Subsequently, cells were fixed with formaldehyde and immunostained as described (Luijsterburg et al. 2012; Helfricht et al. 2013). 20 – 200 cells from two or more independent experiments were analyzed. Antibodies are listed in Supplemental Material.

Statistical analysis

Statistical significance was assessed by a χ2-test (Fig. 1D), a two-tailed Mann-Whitney test (Fig. S2C) or a two-tailed, unpaired t-test (all other figures), and is indicated as **** = $p < 0.0001$, *** = $p < 0.001$, ** = $p < 0.01$, * = $p < 0.05$ and ns = not significant. Average values of two to four independent experiments -/+ SEM are shown.

ACKNOWLEDGEMENTS

The authors would like to thank Nisha Verweij, Jer-gung Chang, Anton de Groot, Andrea Björkman and Steve Jackson for help with cloning experiments, MS sample analysis, MS data analysis, CSR junction analysis and plasmid integration assays, respectively. GFP-XRCC4 was a kind gift from Penny Jeggo. This work was financially supported by grants from the Dutch Scientific Organisation (NWO-VENI; M.S.L. and NWO-VIDI; H.IJ and M.v.d.B.), People Programme - Marie Curie Actions (P.R.), Natural Sciences and Engineering Research Council of Canada (G.M.S.), Dutch Cancer Society (S.M.v.d.M and H.v.A.) and European Research Council (Starting grant; A.C.O.V and Q.P-H., Consolidator; H.v.A.).

REFERENCES

1. Ali AA, Timinszky G, Arribas-Bosacoma R, Kozlowski M, Hassa PO, Hassler M, Ladurner AG, Pearl LH, Oliver AW. 2012. The zinc-finger domains of PARP1 cooperate to recognize DNA strand breaks. Nat Struct Mol Biol 19: 685-692.
2. Alt FW, Zhang Y, Meng FL, Guo C, Schwer B. 2013. Mechanisms of programmed DNA lesions and genomic instability in the immune system. Cell 152: 417-429.
3. Altmeyer M, Neelsen KJ, Teloni F, Pozdnyakova I, Pellegrino S, Grofte M, Rask MB, Streicher W, Jungmichel S, Nielsen ML et al. 2015. Liquid demixing of intrinsically disordered proteins is seeded by poly(ADP-ribose). Nat Commun 6: 8088.
4. Audebert M, Salles B, Calsou P. 2004. Involvement of poly(ADP-ribose) polymerase-1 and XRCC1/DNA ligase III in an alternative route for DNA double-strand breaks rejoining. JBiolChem 279: 55117-55126.
5. Bardwell VJ, Treisman R. 1994. The POZ domain: a conserved protein-protein interaction motif. Genes Dev 8: 1664-1677.
6. Bennardo N, Cheng A, Huang N, Stark JM. 2008. Alternative-NHEJ is a mechanistically distinct pathway of mammalian chromosome break repair. PLoSGenet 4: e1000110.
7. Bjorkman A, Qvist P, Du L, Bartish M, Zaravinos A, Georgiou K, Borglum AD, Gatti RA, Torngren T, Pan-Hammarstrom Q. 2015. Aberrant recombination and repair during immunoglobulin class switching in BRCA1-deficient human B cells. ProcNatlAcadSciUSA 112: 2157-2162.
8. Blanco-Betancourt CE, Moncla A, Milili M, Jiang YL, Viegas-Pequignot EM, Roquelaure B, Thuret I, Schiff C. 2004. Defective B-cell-negative selection and terminal differentiation in the ICF syndrome. Blood 103: 2683-2690.
9. Brochu G, Duchaine C, Thibeault L, Lagueux J, Shah GM, Poirier GG. 1994. Mode of action of poly(ADP-ribose) glycohydrolase. Biochim Biophys Acta 1219: 342-350.
10. Chouery E, Abou-Ghoch J, Corbani S, El AN, Korban R, Salem N, Castro C, Klayme S, Azoury-Abou RM, Khoury-Matar R et al. 2012. A novel deletion in ZBTB24 in a Lebanese family with immunodeficiency, centromeric instability, and facial anomalies syndrome type 2. ClinGenet 82: 489-493.
11. de Greef JC, Wang J, Balog J, den Dunnen JT, Frants RR, Straasheijm KR, Aytekin C, van der Burg M, Duprez L, Ferster A et al. 2011. Mutations in ZBTB24 are associated with immunodeficiency, centromeric instability, and facial anomalies syndrome type 2. AmJHumGenet 88: 796-804.
12. Du L, van der Burg M, Popov SW, Kotnis A, van Dongen JJ, Gennery AR, Pan-Hammarstrom Q. 2008. Involvement of Artemis in nonhomologous end-joining during immunoglobulin class switch recombination. JExpMed 205: 3031-3040.
13. Enervald E, Du L, Visnes T, Bjorkman A, Lindgren E, Wincent J, Borck G, Colleaux L, Cormier-Daire V, van Gent DC et al. 2013. A regulatory role for the cohesin loader NIPBL in nonhomologous end joining during immunoglobulin class switch recombination. JExpMed 210: 2503-2513.
14. Eustermann S, Videler H, Yang JC, Cole PT, Gruszka D, Veprintsev D, Neuhaus D. 2011. The DNA-binding domain of human PARP-1 interacts with DNA single-strand breaks as a monomer through its second zinc finger. JMolBiol 407: 149-170.
15. Hagleitner MM, Lankester A, Maraschio P, Hulten M, Fryns JP, Schuetz C, Gimelli G, Davies EG, Gennery A, Belohradsky BH et al. 2008. Clinical spectrum of immunodeficiency, centromeric instability and facial dysmorphism (ICF syndrome). JMedGenet 45: 93-99.
16. Hansen RS, Wijmenga C, Luo P, Stanek AM, Canfield TK, Weemaes CM, Gartler SM. 1999. The DNMT3B DNA methyltransferase gene is mutated in the ICF immunodeficiency syndrome. ProcNatlAcadSciUSA 96: 14412-14417.
17. Helfricht A, Wiegant WW, Thijssen PE, Vertegaal AC, Luijsterburg MS, van Attikum H. 2013. Remodeling and spacing factor 1 (RSF1) deposits centromere proteins at DNA double-strand breaks to promote non-homologous end-joining. Cell Cycle 12: 3070-3082.
18. Ijspeert H, Driessen GJ, Moorhouse MJ, Hartwig NG, Wolska-Kusnierz B, Kalwak K, Pituch-Noworolska A, Kondratenko I, van Montfrans JM, Mejstrikova E et al. 2014. Similar recombination-activating gene (RAG) mutations result in similar immunobiological effects but in different clinical phenotypes. JAllergy ClinImmunol 133: 1124-1133.
19. Izhar L, Adamson B, Ciccia A, Lewis J, Pontano-Vaites L, Leng Y, Liang AC, Westbrook TF, Harper JW, Elledge SJ. 2015. A Systematic Analysis of Factors Localized to Damaged Chromatin Reveals PARP-Dependent Recruitment of Transcription Factors. Cell Rep 11: 1486-1500.
20. Kalisch T, Ame JC, Dantzer F, Schreiber V. 2012. New readers and interpretations of poly(ADP-ribosyl)ation. Trends BiochemSci 37: 381-390.
21. Langelier MF, Planck JL, Roy S, Pascal JM. 2012. Structural basis for DNA damage-dependent poly(ADP-ribosyl)ation by human PARP-1. Science 336: 728-732.
22. Li M, Lu LY, Yang CY, Wang S, Yu X. 2013. The FHA and BRCT domains recognize ADP-ribosylation during DNA damage response. Genes Dev 27: 1752-1768.
23. Lonskaya I, Potaman VN, Shlyakhtenko LS, Oussatcheva EA, Lyubchenko YL, Soldatenkov VA. 2005. Regulation of poly(ADP-ribose) polymerase-1 by DNA structure-specific binding. J Biol Chem 280: 17076-17083.
24. Lu G, Duan J, Shu S, Wang X, Gao L, Guo J, Zhang Y. 2016. Ligase I and ligase III mediate the DNA double-strand break ligation

in alternative end-joining. Proc Natl Acad Sci U S A 113: 1256-1260.
25. Luijsterburg MS, Acs K, Ackermann L, Wiegant WW, Bekker-Jensen S, Larsen DH, Khanna KK, van Attikum H, Mailand N, Dantuma NP. 2012. A new non-catalytic role for ubiquitin ligase RNF8 in unfolding higher-order chromatin structure. EMBO J 31: 2511-2527.
26. Manis JP, Morales JC, Xia Z, Kutok JL, Alt FW, Carpenter PB. 2004. 53BP1 links DNA damage-response pathways to immunoglobulin heavy chain class-switch recombination. NatImmunol 5: 481-487.
27. Mitchell J, Smith GC, Curtin NJ. 2009. Poly(ADP-Ribose) polymerase-1 and DNA-dependent protein kinase have equivalent roles in double strand break repair following ionizing radiation. IntJRadiatOncolBiolPhys 75: 1520-1527.
28. Moorhouse MJ, van ZD, Ijspeert H, Hiltemann S, Horsman S, van der Spek PJ, van der Burg M, Stubbs AP. 2014. ImmunoGlobulin galaxy (IGGalaxy) for simple determination and quantitation of immunoglobulin heavy chain rearrangements from NGS. BMCImmunol 15: 59.
29. Mortusewicz O, Ame JC, Schreiber V, Leonhardt H. 2007. Feedback-regulated poly(ADP-ribosyl)ation by PARP-1 is required for rapid response to DNA damage in living cells. Nucleic Acids Res 35: 7665-7675.
30. Najafabadi HS, Mnaimneh S, Schmitges FW, Garton M, Lam KN, Yang A, Albu M, Weirauch MT, Radovani E, Kim PM et al. 2015. C2H2 zinc finger proteins greatly expand the human regulatory lexicon. NatBiotechnol 33: 555-562.
31. Nitta H, Unoki M, Ichiyanagi K, Kosho T, Shigemura T, Takahashi H, Velasco G, Francastel C, Picard C, Kubota T et al. 2013. Three novel ZBTB24 mutations identified in Japanese and Cape Verdean type 2 ICF syndrome patients. JHumGenet 58: 455-460.
32. Pan Q, Petit-Frere C, Lahdesmaki A, Gregorek H, Chrzanowska KH, Hammarstrom L. 2002. Alternative end joining during switch recombination in patients with ataxia-telangiectasia. EurJImmunol 32: 1300-1308.
33. Pan-Hammarstrom Q, Jones AM, Lahdesmaki A, Zhou W, Gatti RA, Hammarstrom L, Gennery AR, Ehrenstein MR. 2005. Impact of DNA ligase IV on nonhomologous end joining pathways during class switch recombination in human cells. JExpMed 201: 189-194.
34. Paul K, Wang M, Mladenov E, Bencsik-Theilen A, Bednar T, Wu W, Arakawa H, Iliakis G. 2013. DNA ligases I and III cooperate in alternative non-homologous end-joining in vertebrates. PLoS One 8: e59505.
35. Petersen S, Casellas R, Reina-San-Martin B, Chen HT, Difilippantonio MJ, Wilson PC, Hanitsch L, Celeste A, Muramatsu M, Pilch DR et al. 2001. AID is required to initiate Nbs1/gamma-H2AX focus formation and mutations at sites of class switching. Nature 414: 660-665.
36. Pines A, Mullenders LH, van Attikum H, Luijsterburg MS. 2013. Touching base with PARPs: moonlighting in the repair of UV lesions and double-strand breaks. Trends BiochemSci 38: 321-330.
37. Reina-San-Martin B, Difilippantonio S, Hanitsch L, Masilamani RF, Nussenzweig A, Nussenzweig MC. 2003. H2AX is required for recombination between immunoglobulin switch regions but not for intra-switch region recombination or somatic hypermutation. JExpMed 197: 1767-1778.
38. Robert I, Dantzer F, Reina-San-Martin B. 2009. Parp1 facilitates alternative NHEJ, whereas Parp2 suppresses IgH/c-myc translocations during immunoglobulin class switch recombination. JExpMed 206: 1047-1056.
39. Shah GM, Kandan-Kulangara F, Montoni A, Shah RG, Brind'Amour J, Vodenicharov MD, Affar eB. 2011. Approaches to detect PARP-1 activation in vivo, in situ, and in vitro. Methods MolBiol 780: 3-34.
40. Shieh WM, Ame JC, Wilson MV, Wang ZQ, Koh DW, Jacobson MK, Jacobson EL. 1998. Poly(ADP-ribose) polymerase null mouse cells synthesize ADP-ribose polymers. JBiolChem 273: 30069-30072.
41. Stavnezer J, Bjorkman A, Du L, Cagigi A, Pan-Hammarstrom Q. 2010. Mapping of switch recombination junctions, a tool for studying DNA repair pathways during immunoglobulin class switching. AdvImmunol 108: 45-109.
42. Thijssen PE, Ito Y, Grillo G, Wang J, Velasco G, Nitta H, Unoki M, Yoshihara M, Suyama M, Sun Y et al. 2015. Mutations in CDCA7 and HELLS cause immunodeficiency-centromeric instability-facial anomalies syndrome. Nat Commun 6: 7870.
43. Veuger SJ, Curtin NJ, Richardson CJ, Smith GC, Durkacz BW. 2003. Radiosensitization and DNA repair inhibition by the combined use of novel inhibitors of DNA-dependent protein kinase and poly(ADP-ribose) polymerase-1. Cancer Res 63: 6008-6015.
44. Wang M, Wu W, Wu W, Rosidi B, Zhang L, Wang H, Iliakis G. 2006. PARP-1 and Ku compete for repair of DNA double strand breaks by distinct NHEJ pathways. Nucleic Acids Res 34: 6170-6182.
45. Weemaes CM, van Tol MJ, Wang J, van Ostaijen-ten Dam MM, van Eggermond MC, Thijssen PE, Aytekin C, Brunetti-Pierri N, van der Burg M, Graham DE et al. 2013. Heterogeneous clinical presentation in ICF syndrome: correlation with underlying gene defects. EurJHumGenet 21: 1219-1225.
46. Woodbine L, Gennery AR, Jeggo PA. 2014. The clinical impact of deficiency in DNA non-homologous end-joining. DNA Repair (Amst) 16: 84-96.
47. Xu GL, Bestor TH, Bourc'his D, Hsieh CL, Tommerup N, Bugge M, Hulten M, Qu X, Russo JJ, Viegas-Pequignot E. 1999. Chromosome instability and immunodeficiency syndrome caused by mutations in a DNA methyltransferase gene. Nature 402: 187-191.

SUPPLEMENTAL MATERIALS AND METHODS

Patients

Sera and PBMCs were obtained after informed consent from two ICF2 patients that have been described previously (patients 49 and 55; (Weemaes et al. 2013) and one novel ICF2 patient (p67) carrying the same recessive mutation as patient 49.

Isolation of peripheral blood mononuclear cells and phenotyping of lymphocytes

Peripheral blood mononuclear cells (PBMC) were obtained from patients, family members and healthy donors by Ficoll density gradient separation. PBMC were stored in liquid nitrogen until analysis. Thawed PBMC were stained with the following fluorochrome-labeled antibodies against the indicated cell surface antigen: CD3 (clone #UCHT1) and CD4 (#13B8.2) (Beckman-Coulter); CD8 (#SK1), CD19 (#SJ25C1), CD20 (#L27) CD27 (#L128), CD28 (#L293) and IgM (#G20-127) (BD Biosciences); CCR7 (#150503) (R&D Systems); IgD (rabbit F(ab')2) (DAKO); CD45RA (#MEM-56) (Invitrogen Life Technologies). DAPI (4',6-diamidino-2-phenylindole) was added to discriminate between live and dead cells. Samples were analyzed on a BD Biosciences LSR II flowcytometer with DIVA software.

In vitro B-cell stimulation and analysis of IgG and IgA production

PBMC (0.25 x 106/well) were cultured in a flatbottom 96-well plate in AIM-V medium supplemented with 5% FCS ultra-low IgG, penicillin/streptomycin (100 IU/mL/100 mg/mL; Life Technologies), 0.05 mg/mL transferrin and 5 mg/mL insulin (Sigma-Aldrich). Added stimuli were: MAB89 (aCD40; 0.5 mg/mL; Beckman-Coulter), aIgM (1 mg/mL; Jackson Immunoresearch), CpG (ODN2006; 1 mg/mL; Invivogen) and IL-21 (20 ng/mL; Peprotech). Supernatants were harvested at day 7 and analyzed for IgG and IgA levels by sandwich ELISA using goat anti-human IgG or IgA (Life Technologies) for coating of the 96-well microtiter plates and alkaline phosphatase conjugated goat anti-human IgG or IgA (Life Technologies) for detection.

Immunoglobulin heavy chain (IgH) repertoire analysis using next generation sequencing

The VH-JH rearrangements, Cα and Cγ transcripts were amplified from post-ficoll PBMC in a multiplex PCR using the VH1-6 FR1 and JH consensus BIOMED-2 primers (van Dongen et al. 2003) or a consensus Cα (IGHA-R; 5'-CTTTCGCTCCAGGTCACACTGAG-3') and Cγ primer (3'Cγ-CH1 (Tiller et al., 2008)). The primers were adapted for 454 sequencing by adding the forward A or reverse B adaptor, the 'TCAG' key and multiplex identifier (MID) adaptor. PCR products were purified by gel extraction (Qiagen) and Agencourt AMPure XP beads (Beckman Coulter). DNA concentration was measured using the Quant-it Picogreen dsDNA assay (Invitrogen, Carlsbad, CA). Purified PCR products were sequenced on the 454 GS junior instrument (Roche) according to the manufacturer's recommendations, using the GS Junior Titanium emPCR (Lib-A), GS Junior Titanium sequencing and PicoTiterPlate kits for the VH-JH rearrangements, and the GS Junior+ emPCR (Lib-A), GS Junior sequencing XL+ and PicoTiterPlate kits for the Cα and Cγ transcripts. Using the IGGalaxy Tool (Moorhouse et al. 2014) sequences were demultiplexed based on their MID sequence and quality checked. FASTA files were uploaded in IMGT HighV-Quest (www.imgt.org). Further analysis of the data was done using the IGGalaxy tool. Uniqueness of sequences was defined by V, D and J gene usage and nucleotide sequence of the CDR3 region for the VH-JH rearrangements, and V gene usage, amino acid sequence of the CDR3 region and C gene usage for the Cα

and Cγ transcripts. Only unique, productive sequences were used for the analysis and the frequency of mutated nucleotides in the VH gene was calculated from CDR1 until FR3.

Sequencing of switch recombination junctions
Amplification, cloning and sequencing of the Sm-Sa or Sm-Sg fragments derived from PBMC was performed using a previously described PCR strategy (Pan-Hammarstrom et al. 2005). The CSR junctions were determined by aligning the switch fragment sequences with the reference Sm, Sa or Sg sequences. Analysis of the repair pattern of the CSR junctions was performed based on the suggested guidelines (Stavnezer et al. 2010).

Cell culture
U2OS, HEK293, HEK293T and VH10-SV40-immortalized fibroblast cells were grown in DMEM (Gibco) containing 10% FCS (Bodinco BV) and 1% penicillin/ streptomycin unless stated otherwise. U2OS 2–6–3 cells containing 200 copies of a LacO-containing cassette (~4 Mbp) were gifts from Dr. J. Lukas and Dr. S. Janicki (Doil et al. 2009; Shanbhag et al. 2010) and were used to establish U2OS 2-6-3 cell lines stably expressing GFP-tagged XRCC4 using puromycin selection (1 μg/ml). U2OS 2-6-3 cells stably expressing ER-mCherry-LacR-FokI-DD, which were a gift from Dr. R. Greenberg (Tang et al. 2013), were induced for 5 h by 1 μM Shield-1 (Clontech) and 1 μM 4-OHT (Sigma).

Plasmids
The full-length cDNA of human ZBTB24 was obtained by RT-PCR and flanking restriction sites for conventional cloning (BglII/SalI) were introduced using a nested PCR on the cDNA. The obtained PCR product was subsequently cloned into pEGFP-C1 and pEGFP-N1 (both Clontech) using the BglII and SalI restriction sites. The GST-ZBTB24 expression vector was generated by cloning the ZBTB24 ORF from pEGFP-C1-ZBTB24 as a BglII/ EcoRI fragment into BamHI/EcoRI-digested pGEX-6p-3 (GE Healthcare). The Myc-ZBTB24 expression vector was obtained by exchanging GFP, using the AgeI and BglII restriction sites, for a single Myc tag (EQKLISEEDL) by oligo annealing in the pEGFP-ZBTB24 construct. Deletion constructs were generated by amplifying the specified regions using internal primers containing BglII (forward) or EcoRI (reverse) and subsequent exchange of the deletion fragments for the full length cDNA. All ZBTB24 expression constructs were verified using Sanger sequencing. mCherry-PARG wt/cd were kindly provided by Michael Hendzel (Ismail et al., 2012) and GFP-PARP1 was obtained from Valerie Schreiber (Mortusewicz et al. 2007).
An IRES-Puro cassette was amplified by PCR and inserted into EGFP-C1 (Addgene). The XRCC4 cDNA, a generous gift of P. Jeggo (Girard et al. 2004), was inserted into EGFP-C1-IRES-Puro. Single U2OS clones stably expressing EGFP-XRCC4 were isolated after selection on puromycin (1 mg/ml). Immunoblotting with anti-GFP antibody showed that the XRCC4 fusion proteins were expressed at the expected molecular weight.

Transfections and RNA interference
siRNA and plasmid transfections were performed using Lipofectamine RNAiMAX (Invitrogen), Lipofectamine 2000 (Invitrogen), and JetPEI (Polyplus Transfection), respectively, according to the manufacturer's instructions. siRNA sequences are listed in Table S5. Cells were transfected twice with siRNAs (40 or 80 nM) within 24 h and examined further 48 h after the second transfection unless stated otherwise. PARP inhibitor (KU-0058948) was a gift from Mark O'Connor and was used at a concentration of 10 μM. The DNA-PK inhibitor (NU7026,

EMD Biosciences) was used at a concentration of 10 µM.

Non-homologous end-joining assay
HEK293 cell lines containing a stably integrated copy of the EJ5-GFP reporter were used to measure the repair of I-SceI-induced DSBs or NHEJ (Pierce et al. 1999; Bennardo et al. 2008). Briefly, 48 h after siRNA transfection, cells were transfected with the I-SceI expression vector pCBASce and a mCherry expression vector. 48 h later the fraction of GFP-positive cells among the mCherry-positive cells was determined by FACS on a BD LSRII flow cytometer (BD Bioscience) using FACSDiva software version 5.0.3. Quantifications were performed using Flowing software 2.5.1 (by Perttu Terho in collaboration with Turku Bioimaging).

Plasmid integration assay
Upon siRNA mediated knockdown of the indicated genes, U2OS cells were transfected with XhoI/BamHI-linearized pEGFP-C1 plasmid DNA. After overnight transfection, a fraction of cells was used to determine transfection efficiency, as measured by the amount of GFP positive cells using the ArrayScan high content analysis reader (Thermo Scientific) using the target activation protocol. In parallel cells were seeded on 14 cm plates at a density of 10.000 and 2.000 cells per plate for determination of the cloning efficiency with and without G418 (0.5 mg/ml, Gibco) selection respectively. After 10 days, cells were washed in 0.9% NaCl and stained with methylene blue. NHEJ efficiency was calculated as follows: (cloning efficiency G418 selection) / ((cloning efficiency without selection) x (transfection efficiency)) and subsequently normalized to the luciferase control.

Cell cycle profiling
For cell cycle analysis cells were treated as described in figure legends and fixed in 70% ethanol, followed by DNA staining with 50 µg/ml propidium iodide in the presence of RNase A (0.1 mg/ml). Cell sorting was performed on a flow cytometer (LSRII; BD) using FACSDiva software (version 5.0.3; BD). Quantification was performed using Flowing software 2.5.1.

Cell survival assay
VH10-SV40 cells were transfected with siRNAs, trypsinized, seeded at low density, and exposed to IR at indicated doses. Seven days later cells were washed with 0.9% NaCl and stained with methylene blue. Colonies of more than 10 cells were counted and relative survival compared to the untreated sample was calculated.

RNA expression analysis by RT-qPCR and RNA sequencing
Gene expression analysis using quantitative realtime PCR was carried out as described before (Helfricht et al. 2013). Briefly, RNA isolation was done using the miRNeasy minikit (Qiagen) and subsequently polydT primed cDNA was generated using the RevertAid first strand cDNA synthesis kit (Thermo scientific) according to manufacturer's instructions. Realtime qPCR was performed in duplicate on the CFX96/384 system using SYBR green master mix (Bio-Rad). Primers, which are listed in Table 5S, were designed using Primer3Plus software (http://primer3plus.com). Relative expression levels were obtained with the CFX manager (version 3.0), correcting for primer efficiencies and using GAPDH and GUSB as reference genes. For RNA sequencing, the RNA 6000 Nano kit (Agilent technologies) was used to confirm RNA integrity before the RNA was subjected to poly(A) enrichment. cDNA synthesis, library preparation and sequencing were carried out using the Ion Total RNA-Seq

kit V2, the Ion PI Template OT2 200 Kit v3 and the Ion Sequencing 200 kit v3, respectively, according to the manufacturer's instructions (Thermo Fisher Scientific). RNA was sequenced on an Ion Proton System at a depth of approximately 20 million reads per sample, with a median read length of 90bp. Sequence files obtained in the bam format were converted to fastq using the bam2fastq conversion utility from the bedtools package. Reads were aligned to the human genome build GRCh37 - Ensembl using Tophat2 (Version 2.0.10). In a second alignment step, Bowtie2 (Version 2-2.10) was used in the local, very sensitive mode to align remaining un-aligned reads. HTSeq-Count (Version 0.6.1 was used) with default settings to quantify gene expression. Finally, DESeq (Version 1.2.10) was used to generate a list of genes differentially expressed between ZBTB24-depleted and control cells (Table S2).

Sample preparation and mass spectrometry

For stable isotope labeling by amino acids in cell culture (SILAC), U2OS cells were cultured for 14 days in light (L) ([12C6,14N2]lysine/[12C6,14N4]arginine) or heavy (H) ([13C6,15N2] lysine/[13C6,15N4]arginine) SILAC medium. SILAC-labeled cells were transiently transfected with either GFP-PARP1 or GFP-ZBTB24 (H) and an empty vector (L). Equal amounts of H and L cells were lysed separately in EBC-150 buffer (50 mM Tris-HCl pH 7.5, 150 mM NaCl, 0.5% NP-40, 1 mM EDTA) supplemented with protease and phosphatase inhibitor cocktails. The lysed cell suspension was sonicated 6 times for 10s on ice and subsequently incubated with 500 U Benzonase for 1 hour under rotation. The NaCl concentration was increased to 300 mM and the cleared lysates were subjected to GFP immunoprecipitation with GFP Trap beads (Chromotek). The beads were then washed 2 times with EBC-300 buffer (50 mM Tris, pH 7.5, 300 mM NaCl, 0.5% NP-40, 1 mM EDTA) and 2 times with 50 mM (NH4)2CO3 followed by overnight digestion using 2.5 µg trypsin at 37°C under constant shaking. Peptides of the H and L precipitates were mixed and desalted using a Sep-Pak tC18 cartridge by washing with 0.1 % acetic acid. Finally, peptides were eluted with 0.1 % acetic acid/60 % acetonitrile and lyophilized. Samples were analyzed by nanoscale LC-MS/MS using an EASY-nLC system (Proxeon) connected to a Q-Exactive Orbitrap (Thermo). Peptides were separated in a 13 cm analytical column with inner-diameter of 75 µm, in-house packed with 1.8 µm C18 beads (Reprospher, Dr. Maisch). The gradient length was 120 minutes with a flow rate of 200nL/minutes. Data dependent acquisition was used with a top 10 method. Full-scan MS spectra were acquired at a target value of 3 x 106 and a resolution of 70,000, and the Higher-Collisional Dissociation (HCD) tandem mass spectra (MS/MS) were recorded at a target value of 1 x 105 and with resolution of 17,500 with a normalized collision energy (NCE) of 25%. The precursor ion masses of scanned ions were dynamically excluded (DE) from MS/MS analysis for 60 sec. Ions with charge 1, and greater than 6 were excluded from triggering MS2 events (Hendriks et al. 2014). Analysis of raw data was performed using MaxQuant software (Cox and Mann 2008).

Protein interaction studies

To study ZBTB24 interactions, cells expressing the indicated GFP fusion proteins were lysed in 1 ml EBC buffer (50 mM Tris, pH 7.3, 150 mM NaCl, 0.5% NP-40, 2.5 mM MgCl) supplemented with protease and phosphatase inhibitor cocktails (Roche). Lysis and protein extraction were enhanced by 6 x 10" sonication in a sonicator bath (Bioruptor UCD-20, Diagenode, Liège, Belgium) followed by 1 hour incubation with 500 units benzonase (Novagen) on ice. Upon centrifugation, cleared lysates were subjected to immunoprecipitation with GFP Trap beads (Chromotek) for 1.5 h at 40C top over top. Beads were washed 6 times with cold EBC buffer,

boiled in Laemmli buffer and interacting proteins were visualized using western blot analysis.

Western blot analysis
Protein extracts were generated by direct lysis of cells in 2x Laemmli buffer and boiled for 10' at 950C. Proteins were size separated using Novex 4-12% Bis-Tris mini gels (Invitrogen) or 4–12% Criterion XT Bis-Tris gels (Bio-rad) in 1x MOPS buffer (Invitrogen) and transferred to PVDF membranes, which were blocked in 4% milk for at least 30 minutes and incubated with the indicated antibodies overnight. Several wash steps before and after 1 h incubation with secondary antibodies rabbit-anti-700 and mouse-anti-800 (Sigma) were executed. Protein bands were visualized using the Odyssey infrared imaging system or the C-Digit blot scanner (both Licor) according to manufacturer's instructions.

Laser micro-irradiation
Multiphoton laser micro-irradiation was performed on a Leica SP5 confocal microscope equipped with an environmental chamber set to 37°C and 5% CO2 as described (Helfricht et al. 2013). Briefly, U20S cells were grown on 18 mm glass coverslips and media was replaced with colorless DMEM or CO2-independent Leibovitz L15 medium, both supplemented with 10% FCS and pen/strep. Cells were placed in a Chamlide TC-A live-cell imaging chamber before imaging and were kept at 37°C. DSB-containing tracks (1 or 1.5 µm width) were generated with a Mira modelocked Ti:Sapphire laser (λ = 800 nm, pulselength = 200 fs, repetition rate = 76 MHz, output power = 80 mW). Typically, cells were micro-irradiated with 1 iteration per pixel using LAS-AF software. For live cell imaging, confocal images were recorded before and after laser irradiation at different time intervals. For UV-A laser micro-irradiation U2OS cells were sensitized with 10 µM 5-bromo-2-deoxyuridine (BrdU) for 24 h, as described (Helfricht et al. 2013). For micro-irradiation, the cells were placed on the stage of a Leica DM IRBE widefield microscope stand (Leica) integrated with a pulsed nitrogen laser (Micropoint Ablation Laser System, Photonic Instruments, Inc; 16 Hz, 364 nm), which was directly coupled to the epifluorescence path of the microscope and focused through a Leica 40× HCX PLAN APO 1.25–0.75 oil-immersion objective. The laser output power was set to 78 to generate strictly localized sub-nuclear DNA damage and images were taken before and after micro-irradiation at the indicated time-points or after immunofluorescent labeling using Andor IQ software.

Immunofluorescent labeling
Immunofluoresecent labeling of γH2AX and XRCC4 was performed as described previously (Helfricht et al. 2013). Briefly, cells were grown on glass coverslips and treated as indicated in the figure legends. Subsequently, cells were washed with PBS, fixed with 4% formaldehyde for 15 min and treated with 0.25% Triton X-100 in PBS for 5 min. Cells were rinsed with PBS and equilibrated in WB (PBS containing 5 g BSA/L, 1.5 g glycine/L) prior to immunostaining. Detection was done using goat anti-mouse or goat anti-rabbit IgG coupled to Alexa 488, 555 or 647 (Invitrogen Molecular probes). Samples were incubated with 0.1 µg/ml DAPI and mounted in Polymount.

Microscopy analysis
Images of fixed samples were acquired on a Zeiss AxioImager M2 or D2 widefield fluorescence microscope equipped with 40×, 63×, and 100× PLAN APO (1.4 NA) oil-immersion objectives (Zeiss) and an HXP 120 metal-halide lamp used for excitation. Fluorescent probes were

detected using the following filters: DAPI (excitation filter: 350/50 nm, dichroic mirror: 400 nm, emission filter: 460/50 nm), GFP/Alexa 488 (excitation filter: 470/40 nm, dichroic mirror: 495 nm, emission filter: 525/50 nm), mCherry (excitation filter: 560/40 nm, dichroic mirror: 585 nm, emission filter: 630/75 nm), Alexa 555 (excitation filter: 545/25 nm, dichroic mirror: 565 nm, emission filter: 605/70 nm), Alexa 647 (excitation filter: 640/30 nm, dichroic mirror: 660 nm, emission filter: 690/50 nm). Images recorded after multi-photon- and UV-A-laser micro-irradiation and immunofluorescence stainings were analyzed using ImageJ. The average pixel intensity of laser tracks induced by either the multi-photon- or the UV-A laser system was measured within the locally irradiated area (Idamage), in the nucleoplasm outside the locally irradiated area (Inucleoplasm) and in a region not containing cells in the same field of view (Ibackground) using ImageJ. The relative level of accumulation expressed relative to the protein level in the nucleoplasm was calculated as follows: ((Idamage − Ibackground)/(Inucleoplasm − Ibackground) – 1). The accumulation in the control cells transfected with siLUC within each experiment was normalized to 100%. Images obtained from live cell imaging after multi-photon micro-irradiation were analyzed using LAS-AF software. Fluorescence intensities were subtracted by the pre-bleach values and normalized to the first data point, which was set to 0, to obtain relative fluorescence units (RFU). The average reflects the quantification of between 50–150 cells from 2–3 independent experiments.

Antibodies

Immunofluorescence and western blot analysis were performed using antibodies against GFP (1:1000, #11814460001, Roche), PARP1 (1:1000, #9542, Cell Signaling, Alexis), Myc (1:1000, 9E10, SC-40, Santa Cruz), γH2AX (1:1000, #07-164, Millipore), α-Tubulin (Sigma), DNA-PKcs (1:500, ab1832, Abcam), LIG4 (1:1000, #80514, Abcam), XRCC4 (1:500, gift from Mauro Modesti), Histone H3 (1:2000, #1791, Abcam), GST (1:2000, Amersham), PARP1 (1:1000, #9542S, Cell Signaling), PARP2 (1:500, #C3956, Sigma), PAR (1:1000, #4336-BPC-100, Trevigen; used in Fig. 5A-B) and PAR monoclonal 10H, which was purified from the culture medium of 10H hybridoma obtained from Dr. Miwa through the Riken cell ban (Kawamitsu et al. 1984).

GST protein purification

For GST purifications 50 ml cultures of E. coli BL21 cells containing pGEX or pGEX-ZBTB24 plasmid were grown to an OD600 of 0.6 absorbance units. 2 mM IPTG was added and cells were incubated overnight at 20 °C. After centrifugation cell pellets were frozen and stored at -80 °C. For protein purification cell pellets were lysed at room temperature for 30 minutes in 2.5 ml lysis buffer (125 mM Tris-HCl pH 8, 150 mM NaCl, 1 mM MgCl2, 5 mM DTT, 0.1 volume BugBuster 10x (Novagen-Merck), 2500 units rLysozyme (Novagen-Merck), 62.5 units benzonase (Novagen-Merck), Protease Inhibitor Cocktail EDTA-free (Sigma-Aldrich)). The lysate was centrifuged at 4 °C in a table centrifuge for 10 minutes at full speed. Supernatant was taken and incubated with 500 µl Glutathione Superflow Agarose beads (Life Technologies) for 2 hrs at 4 °C. The Agarose beads were packed in a column and loaded on an ÅKTA chromatography system (GE Healthcare Biosciences). The column was rinsed using a wash buffer (125 mM Tris-HCl pH8, 150 mM NaCl, 10 mM β-mercaptoethanol) and eluted using wash buffer supplemented with 10 mM reduced glutathione (Sigma-Aldrich). Fractions with purified protein were collected and concentrated using 50kD Vivaspin ultrafiltration cups (Sartorius). Finally, the buffer was changed in ultrafiltration cups to 125

mM Tris-HCl pH8, 150 mM NaCl, 10% glycerol, and purified proteins were frozen in liquid nitrogen and stored at -80 °C.

Analysis of protein PARylation

Cells were washed with ice-cold PBS supplemented with PARG inhibitor (PARGi; 400 nM Tannic acid), scraped in a small volume of PBS with PARGi and transferred to low binding tubes, followed by high speed centrifugation at 4°C. Cells were lysed in RIPA buffer (10 mM Tris-HCl (pH 8), 1% Triton X-100, 0.1% deoxycholate, 0.1% SDS, 100 µM Tannic acid) supplemented with protease and phosphatase inhibitor cocktails (Roche) comprising a NaCl-concentration of 450 mM. After centrifugation, cleared lysates were subjected to immunoprecipitation with GFP Trap beads (Chromotek) for 2 hours on a rotating wheel in the presence of 150 mM NaCl. Beads were washed 6 times with RIPA buffer containing increasing NaCl concentrations (150 mM and 1 M) followed by 2 washes with TBS-T buffer (20x TBS, 0.1% Tween, 100 µm Tannic acid). After boiling in Laemmli buffer the interacting proteins were visualized using western blot analysis.

Production of radiolabeled PAR

PARP1 activation assays were carried out as described earlier (Shah et al. 2011) with minor modifications. To prepare radiolabeled PAR, purified bovine PARP1 was activated at 30°C for 30 min in 900 µl reaction mix (100 mM Tris-HCl pH 8.0, 10mM MgCl2, 10 % glycerol, 10 mM DTT, 500 µM cold NAD, 250 µCi of 32P-NAD (350 nM), 10% ethanol and 23 µg activated calf thymus DNA). Auto-PARylated PARP1 was precipitated on ice for at least 30 min by addition of 100 µl 3 M Na-acetate pH 5.2 and 700 µl isopropanol. After centrifugation, pellet was washed twice with ethanol, air-dried and dissolved (1M KOH, 50 mM EDTA), while heating at 60°C for 1 h. Upon addition of AAGE9 (250 mM NH4OAc, 6 M guanidine-HCl, 10 mM EDTA), pH was adjusted to 9.0 and solution was loaded onto DHBB resin in Econocolumns (BioRad). Resin was washed with AAGE9 and NH4-acetate pH 9.0. The polymer was eluted with water at 37°C in separate fractions and stored at -30°C till usage in southwestern assays.

Southwestern assay

The southwester assay was carried out as described (Robu et al. 2013). Briefly, IP samples were resolved on 8% denaturing PAGE gels along with purified human PARP1 (Aparptosis) as a positive control. Gels were incubated for 1 h with gentle agitation in SDS-PAGE running buffer (20-30 ml 25 mM Tris 7.5, 192 mM glycine, 5 % β-mercaptoethanol, 0.1% SDS) followed by protein transfer to a nitrocellulose membrane at 4°C. Membrane were rinsed three times with TST buffer (10 mM Tris pH 7.5, 150 mM NaCl, 0.05 % Tween) and incubated in 20 ml TST buffer supplemented with 250 nM radioactive PAR polymer on a shaker at room temperature for 1 h, followed by three washes with TST and one wash with TST buffer containing 500 mM NaCl. After a final wash with regular TST, membranes were dried and either exposed to a film or a phosphoimager screen to detect radioactivity. Afterwards membranes were blocked in 5 % milk containing 0.1 % Tween and probed for PARP and GFP with the indicated antibodies.

PARP1 activation assays

To examine the stimulatory effect of ZBTB24 on the catalytic activity of PARP1, PARP1 activation reactions were carried out in a 20 µl assay volume with 0.4 pmol of PARP1, 160 ng activated DNA and 100 µM unlabeled NAD at 30°C for 10 min with no other protein (control)

or varying molar ratios of GST-ZBTB24 or GST over PARP1. The reactions were stopped by the addition of equal volumes of 2x Laemmli buffer. Aliquots from each sample were resolved on 6 or 10 % SDS-PAGE followed by immunoblotting for PAR, PARP1 and GST.

PAR protection assays

To examine the effect of ZBTB24 on PAR protection, PARP1 activation reactions were carried out in a 15 µl assay volume with 4 pmol of PARP1, 3 µg of activated and 100 µM unlabeled NAD at 30°C for 30 min to allow the formation of autoPARylated PARP1. The reaction was stopped by the addition of 1 µl of 1 mM PARPi (PJ-34). 1/10th of the reaction mixes containing 0.4 pmols of PARP1 were reacted for 15 min with no other protein (control) or varying molar ratios of GST-ZBTB24 or GST over PARP1. All samples were reacted at 30°C for 15 min in the PARG-assay buffer (50 mM Tris-Cl pH 7.5 containing 50 mM KCl, 1.5 mM DTT, 0.1 mg/ml BSA, 2.5 mM EDTA) with 5 ng PARG (Sigma), whereas the undigested PAR samples were mock-treated with PARG assay buffer. The reactions were stopped by the addition of equal volumes of 2X Laemmli buffer. Aliquots from each sample were resolved on 6 or 10 % SDS-PAGE followed by immunoblotting for PAR, PARP1 and GST.

SUPPLEMENTAL REFERENCES

1. Bennardo N, Cheng A, Huang N, Stark JM. 2008. Alternative-NHEJ is a mechanistically distinct pathway of mammalian chromosome break repair. PLoSGenet 4: e1000110.
2. Cox J, Mann M. 2008. MaxQuant enables high peptide identification rates, individualized p.p.b.-range mass accuracies and proteome-wide protein quantification. NatBiotechnol 26: 1367-1372.
3. Doil C, Mailand N, Bekker-Jensen S, Menard P, Larsen DH, Pepperkok R, Ellenberg J, Panier S, Durocher D, Bartek J et al. 2009. RNF168 binds and amplifies ubiquitin conjugates on damaged chromosomes to allow accumulation of repair proteins. Cell 136: 435-446.
4. Girard PM, Kysela B, Harer CJ, Doherty AJ, Jeggo PA. 2004. Analysis of DNA ligase IV mutations found in LIG4 syndrome patients: the impact of two linked polymorphisms. HumMolGenet 13: 2369-2376.
5. Helfricht A, Wiegant WW, Thijssen PE, Vertegaal AC, Luijsterburg MS, van Attikum H. 2013. Remodeling and spacing factor 1 (RSF1) deposits centromere proteins at DNA double-strand breaks to promote non-homologous end-joining. Cell Cycle 12: 3070-3082.
6. Hendriks IA, D'Souza RC, Yang B, Verlaan-de VM, Mann M, Vertegaal AC. 2014. Uncovering global SUMOylation signaling networks in a site-specific manner. NatStructMolBiol 21: 927-936.
7. Kawamitsu H, Hoshino H, Okada H, Miwa M, Momoi H, Sugimura T. 1984. Monoclonal antibodies to poly(adenosine diphosphate ribose) recognize different structures. Biochemistry 23: 3771-3777.
8. Moorhouse MJ, van ZD, Ijspeert H, Hiltemann S, Horsman S, van der Spek PJ, van der Burg M, Stubbs AP. 2014. ImmunoGlobulin galaxy (IGGalaxy) for simple determination and quantitation of immunoglobulin heavy chain rearrangements from NGS. BMCImmunol 15: 59.
9. Mortusewicz O, Ame JC, Schreiber V, Leonhardt H. 2007. Feedback-regulated poly(ADP-ribosyl)ation by PARP-1 is required for rapid response to DNA damage in living cells. Nucleic Acids Res 35: 7665-7675.
10. Murray JE, van der Burg M, Ijspeert H, Carroll P, Wu Q, Ochi T, Leitch A, Miller ES, Kysela B, Jawad A et al. 2015. Mutations in the NHEJ component XRCC4 cause primordial dwarfism. AmJHumGenet 96: 412-424.
11. Pan-Hammarstrom Q, Jones AM, Lahdesmaki A, Zhou W, Gatti RA, Hammarstrom L, Gennery AR, Ehrenstein MR. 2005. Impact of DNA ligase IV on nonhomologous end joining pathways during class switch recombination in human cells. JExpMed 201: 189-194.
12. Pierce AJ, Johnson RD, Thompson LH, Jasin M. 1999. XRCC3 promotes homology-directed repair of DNA damage in mammalian cells. Genes Dev 13: 2633-2638.
13. Robu M, Shah RG, Petitclerc N, Brind'Amour J, Kandan-Kulangara F, Shah GM. 2013. Role of poly(ADP-ribose) polymerase-1 in the removal of UV-induced DNA lesions by nucleotide excision repair. ProcNatlAcadSciUSA 110: 1658-1663.
14. Shah GM, Kandan-Kulangara F, Montoni A, Shah RG, Brind'Amour J, Vodenicharov MD, Affar eB. 2011. Approaches to detect PARP-1 activation in vivo, in situ, and in vitro. Methods MolBiol 780: 3-34.
15. Shanbhag NM, Rafalska-Metcalf IU, Balane-Bolivar C, Janicki SM, Greenberg RA. 2010. ATM-dependent chromatin changes silence transcription in cis to DNA double-strand breaks. Cell 141: 970-981.
16. Stavnezer J, Bjorkman A, Du L, Cagigi A, Pan-Hammarstrom Q. 2010. Mapping of switch recombination junctions, a tool for studying DNA repair pathways during immunoglobulin class switching. AdvImmunol 108: 45-109.
17. Tang J, Cho NW, Cui G, Manion EM, Shanbhag NM, Botuyan MV, Mer G, Greenberg RA. 2013. Acetylation limits 53BP1 association with damaged chromatin to promote homologous recombination. Nat Struct Mol Biol 20: 317-325.
18. van Dongen JJ, Langerak AW, Bruggemann M, Evans PA, Hummel M, Lavender FL, Delabesse E, Davi F, Schuuring E, Garcia-Sanz R et al. 2003. Design and standardization of PCR primers and protocols for detection of clonal immunoglobulin and T-cell receptor gene recombinations in suspect lymphoproliferations: report of the BIOMED-2 Concerted Action BMH4-CT98-3936. Leukemia 17: 2257-2317.
19. Weemaes CM, van Tol MJ, Wang J, van Ostaijen-ten Dam MM, van Eggermond MC, Thijssen PE, Aytekin C, Brunetti-Pierri N, van der Burg M, Graham DE et al. 2013. Heterogeneous clinical presentation in ICF syndrome: correlation with underlying gene defects. EurJHumGenet 21: 1219-1225.

SUPPLEMENTAL FIGURES

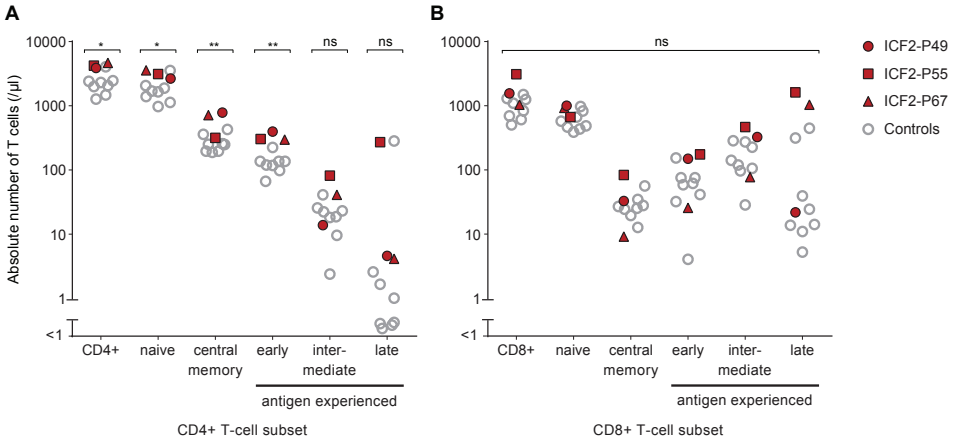

Figure S1. T-cell differentiation in ICF2 patients (related to Fig. 1)**.** Absolute numbers (per µL) of the peripheral blood CD3+CD4+ T-cell subset (A) and CD3+CD8+ T-cell subset (B) and the indicated differentiation stages in both subsets were determined in the ICF2 patients P49, P55 and P67 (closed red symbols) and eight healthy age-matched controls (open grey circles, age range 0.8 to 4.3 years) by flow cytometry. These studies were performed with patient PBMC obtained at the age of 0.9, 0.8 and 3.6 years, respectively. Phenotypical definitions: naïve T cells: CD45RA+CCR7+; central memory T cells: CD45RA-CCR7+; antigen experienced CD4+ T cells CD45RA-/+CCR7-: early CD28+CD27+; intermediate CD28+CD27-; late CD28-CD27-; antigen experienced CD8+ T cells CD45RA-/+CCR7-: early CD28+CD27+; intermediate CD28-CD27+; late CD28-CD27-.

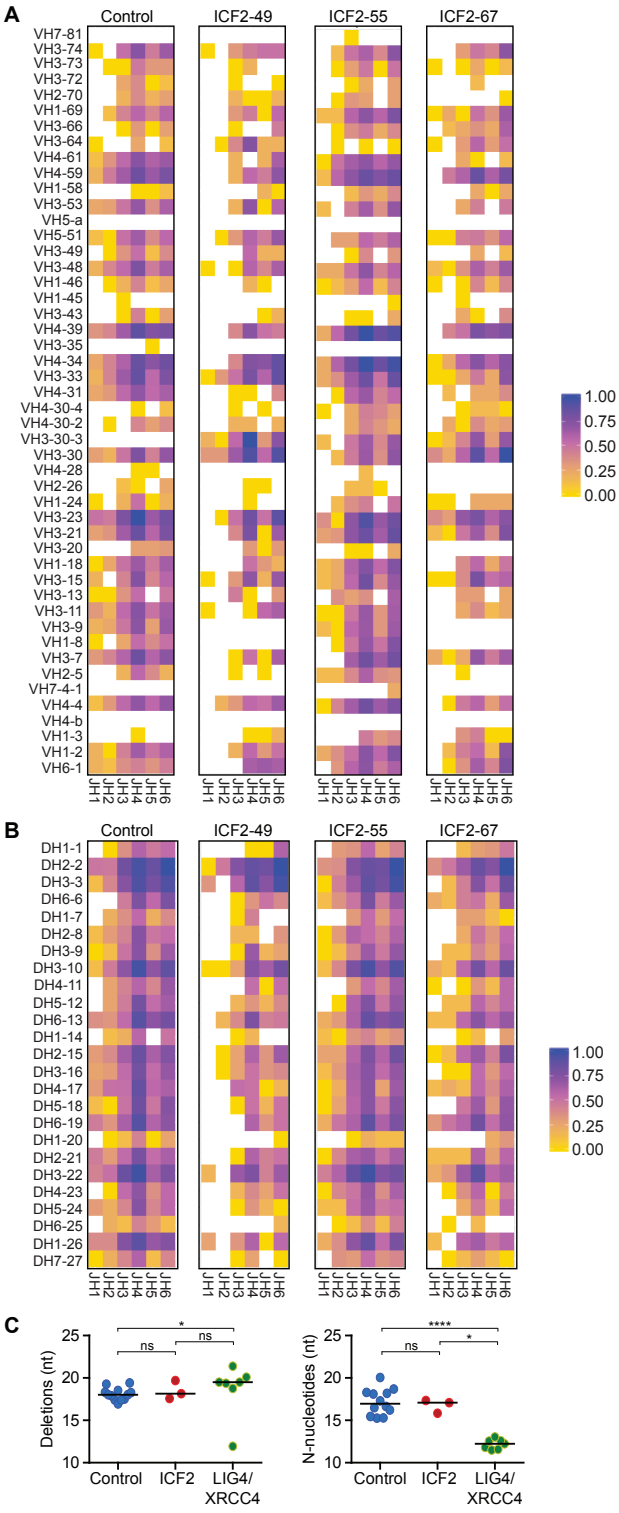

Figure S2. Combinational diversity and junction characteristics of IgH rearrangements (related to Fig. 1). Heatmaps showing the relative frequency of the combinational diversity of (A) VH and JH genes or (B) DH and JH genes of unique productive IgH rearrangements (defined by the unique combination of VH, DH, JH and nucleotide sequences of CDR3) amplified from control (n=4789) and ICF2 patients ICF2-49 (n=757), IFC2-55 (n=3723) and ICF2-67 (n=1663). (C) The ICF2 patients display normal numbers of deletions and N-nucleotides compared to control (n=12), in contrast to XRCC4- and LIG4-deficient patients (n=7) (Murray et al. 2015), who display increased numbers of deletions and decreased numbers of N-nucleotides in unique unproductive IGH rearrangements.

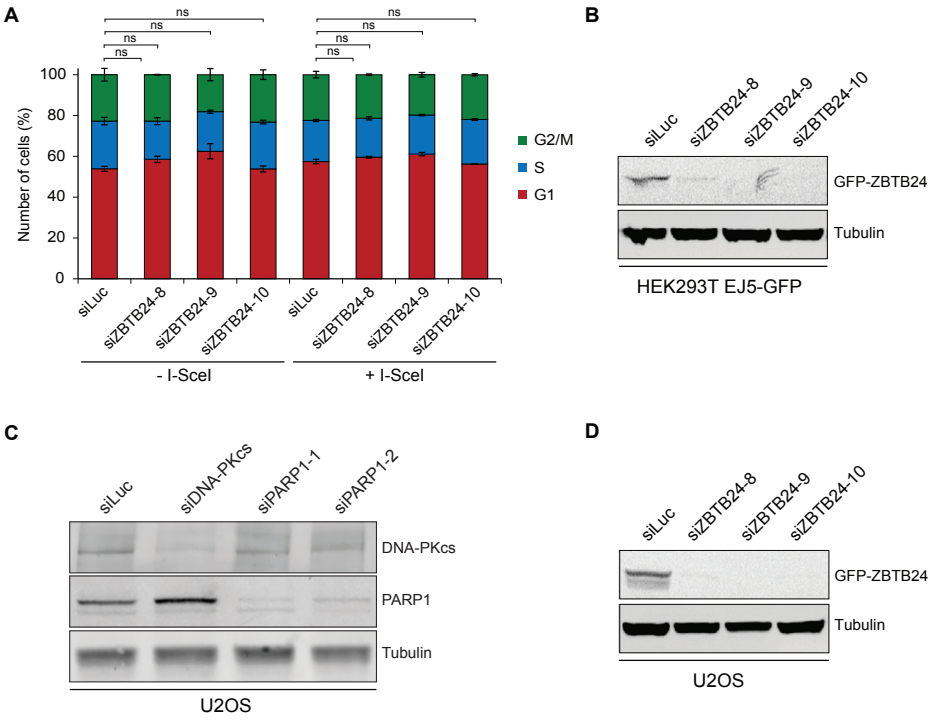

Figure S3. Knockdown of ZBTB24 does not affect cell cycle progression (related to Fig. 2). (A) HEK293T cells containing the EJ5-GFP reporter were transfected with the indicated siRNAs. 48 h later cells were transfected with a control vector or the I-SceI expression vector (pCBASce). After an additional 24 h cells were subjected to propidium iodide staining followed by flow cytometry analysis. The percentage of cells in G1 (red bar), S (blue bar) and G2/M (green bar) phase is presented. (B) HEK293T EJ5-GFP cells were treated with the indicated siRNAs. 48 h later, cells were transiently transfected with GFP-ZBTB24. WCEs were prepared 24 h later and subjected to western blot analysis for GFP. Tubulin is a loading control. (C) U2OS cells were treated with the indicated siRNAs. WCEs were prepared 48 h later and subjected to western blot analysis for DNA-PKcs and PARP1. Tubulin is a loading control. (D) As in B, except that U2OS cells were used.

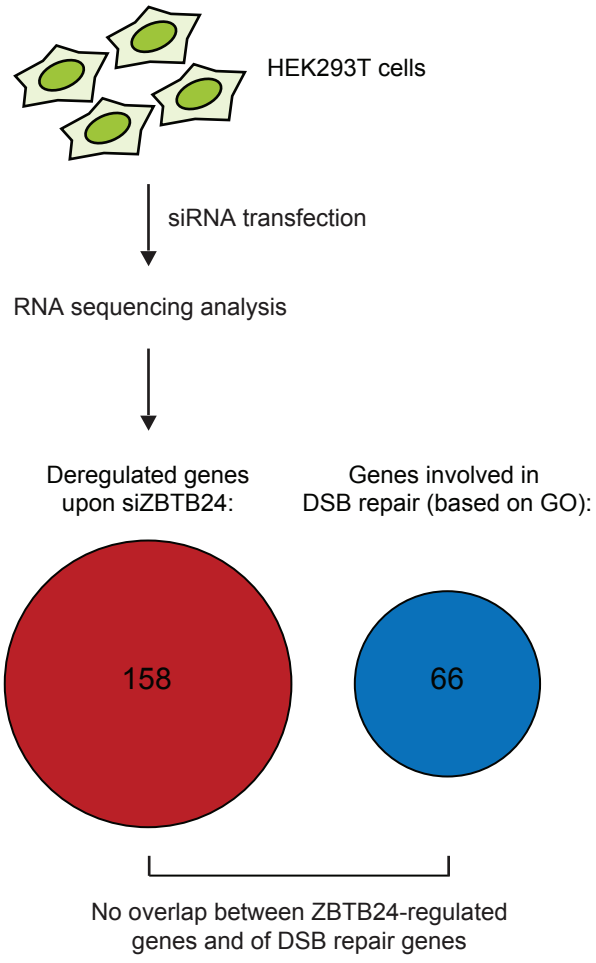

Figure S4. ZBTB24 does not regulate the expression of genes involved in DSB repair (related to Fig. 2). HEK293T cells were treated with control siRNAs against Luciferase or 3 different siRNAs against ZBTB24. Four days later RNA was isolated and subjected to RNA sequencing analysis. The number of genes found to be commonly misregulated following ZBTB24-depletion with each of the siRNAs is presented (FDR < 0.05). Importantly, GO-term term analysis (0006302; DSB repair) did not reveal the presence of DSB repair genes among the misregulated genes.

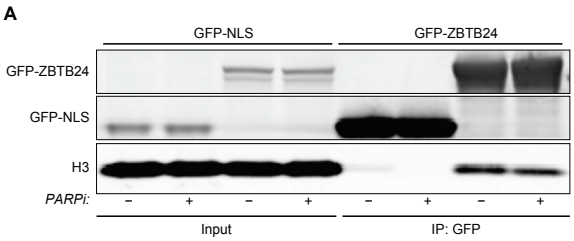

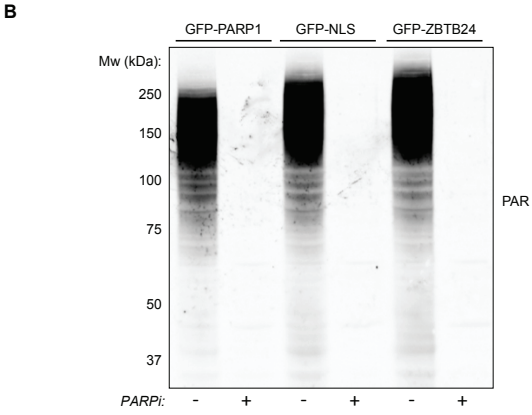

Figure S5. ZBTB24 interacts with histone H3 (related to Fig. 3). (A) U2OS cells transiently expressing GFP-ZBTB24 or GFP-NLS were either treated with DMSO (Mock) or with PARPi. WCEs were subjected to GFP-IP followed by western blot analysis of the indicated proteins. (B) U2OS cells transfected with the indicated GFP-tagged proteins were either treated with DMSO (Mock) or PARPi. WCEs were prepared and subjected to western blot analysis to assess total PAR levels.

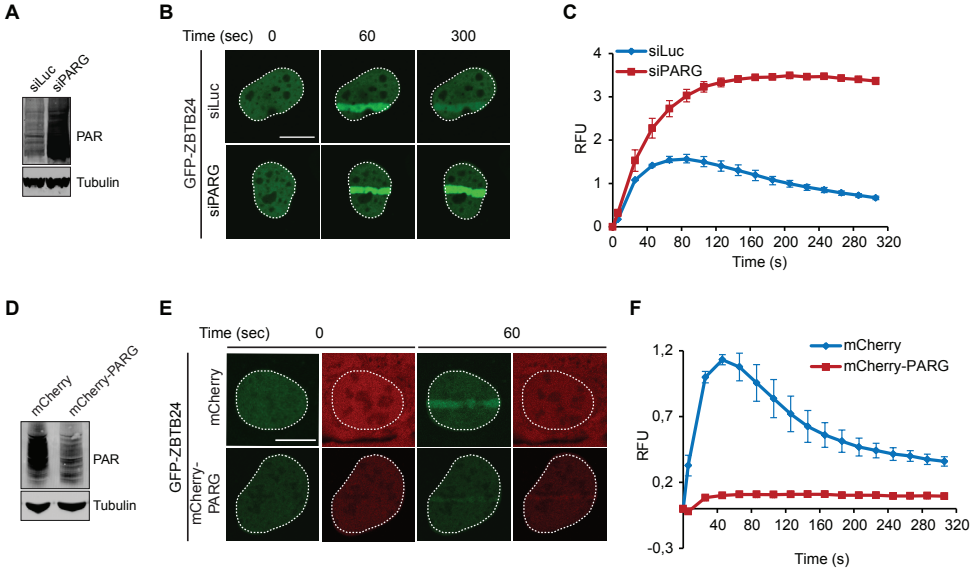

Figure S6. PARG-dependent turnover of PAR chains modulates the accumulation of ZBTB24 at sites of DNA damage (related to Fig. 3). (A) Western blot analysis showing total PAR levels in U2OS cells transfected with the indicated siRNAs and transiently expressing GFP-ZBTB24. Tubulin is loading control. (B) GFP-ZBTB24 accumulation as monitored at the indicated time points after laser micro-irradiation in cells from A. (C) Quantification of the results from B. RFU is Relative Fluorescent Units. (D) As in A, except that cells were co-transfected with a GFP-ZBTB24 and either a mCherry or mCherry-PARG expression vector were used. (E) As in B, expect that cells from D were used. (F) Quantification of the results from E. Scale bar 10 µm.

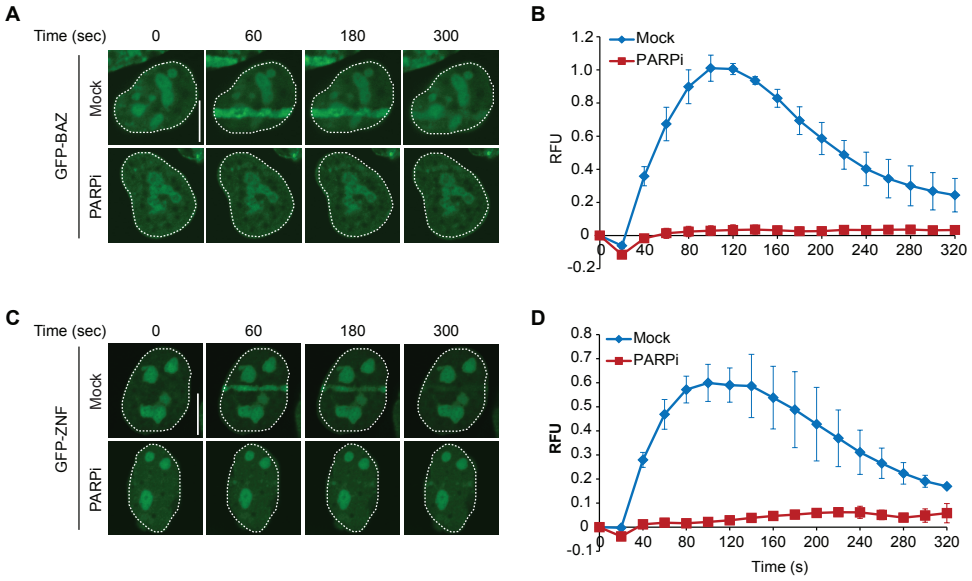

Figure S7. The ZNF domain of ZBTB24 accumulates at sites of DNA damage in a PARP-dependent manner (related to Fig. 4). (A) U2OS cells transiently expressing GFP-tagged BAZ domains of ZBTB24 were treated with DMSO (Mock) or PARPi, and subjected to laser micro-irradiation to follow GFP-BAZ accumulation at sites of DNA damage at the indicated time points after irradiation. Representative images are shown. RFU is Relative Fluorescence Units. Scale bar 10 µm. (B) Quantification of A. (C) As in A, except for the GFP-tagged ZNF domain of ZBTB24 (GFP-ZNF). (D) Quantification of C.

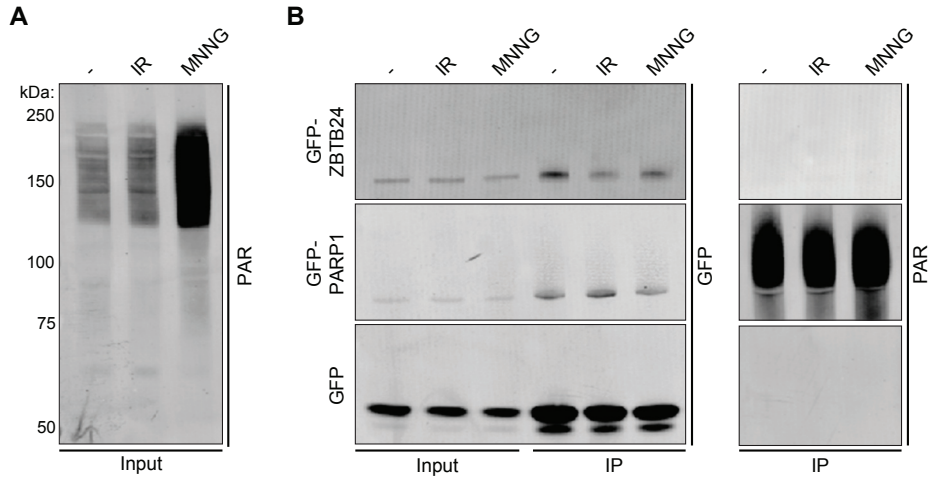

Figure S8. ZBTB24 is not PARylated following DNA damage induction (related to Fig. 4). (A) U2OS cells expressing GFP were left untreated, or treated with IR or MNNG. WCE were prepared and subjected to western blot analysis for global PAR levels. (B) WCE extracts from A and from cells expressing GFP-ZBTB24 or GFP-PARP1 were subjected to GFP-IP. Washes were performed under high-salt conditions to remove interacting proteins. Western blot analysis was done for the indicated proteins and PAR. The experiment was performed 2 times for PARP1 and 4 times for ZBTB24. Blots from a representative experiment are show.

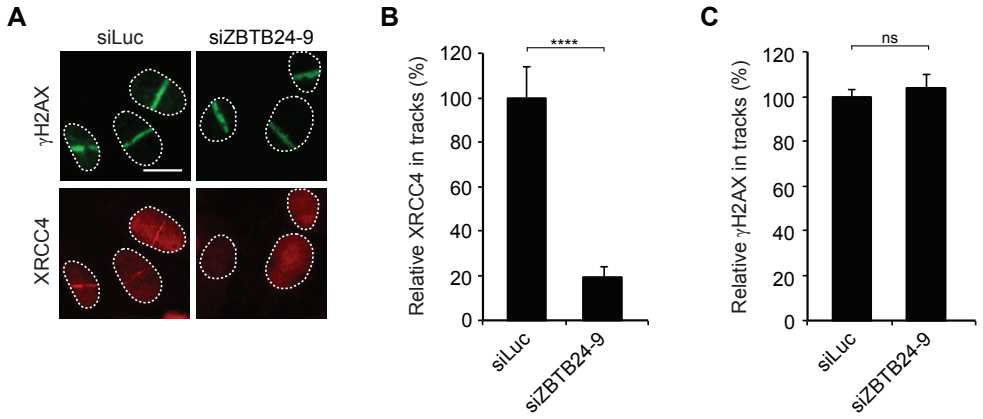

Figure S9. ZBTB24 promotes the recruitment of endogenous XRCC4 to sites of DNA damage (related to Fig. 6). (A) Accumulation of γH2AX and endogenous XRCC4 at sites of laser-inflicted DNA damage. U2OS cells were treated with the indicated siRNAs, subjected to laser micro-irradiation and 10 minutes later fixed and immunostained for γH2AX and endogenous XRCC4. (B) Quantification of endogenous XRCC4 levels in laser tracks from A. (C) As in B, except for γH2AX. Scale bar 10 µm.

Tabel S1: Serum Ig isotype concentrations at first analysis

Patient	Age (m)	IgG (g/L)	Normal range	IgM (g/L)	Normal range	IgA (g/L)	Normal range
ICF2-P49	6 66	1.15 n.d.	3.16-11.48	n.d. <0.04	0.65-2.82	n.d. <0.06	0.34-3.39
ICF2-P55	6 24	1.45 n.d.	3.16-11.48	n.d. <0.04	0.63-2.51	n.d. <0.06	0.23-1.23
ICF2-P67	9	<0.33	3.16-11.48	<0.04	0.47-2.04	<0.07	0.13-0.69

The range of age-dependent normal values (g/L) represents the 5th and 95th percentiles, respectively (Kanariou et al., 1995). m: month, n.d.: not detectable.

Tabel S2: List of ZBTB24-regulated genes identified by RNA-seq

HEK293T cells were transfected with siRNAs against Luciferase or ZBTB24 (siZBTB24-8, siZBTB24-9 or siZBTB24-10) and subjected to RNA-seq. Genes whose expression was affected following treatment with each of the siRNAs against ZBTB24 are shown.

Ensembl.Gene.ID	Associated Gene Name	Fold Change	log2 Fold Change	pval	padj
ENSG00000100292	HMOX1	0,242319408	-2,045018134	2,83908E-05	0,018667905
ENSG00000005102	MEOX1	0,323998217	-1,625942223	3,65729E-07	0,001132639
ENSG00000145721	LIX1	0,340926569	-1,552467058	1,61882E-05	0,014854462
ENSG00000230171	RPL22P18	0,356349218	-1,488636337	2,18977E-05	0,016693086
ENSG00000248979	LAMTOR3P2	0,398942805	-1,325746168	6,25567E-05	0,029242879
ENSG00000232027	RP11-275F13.3	0,406609005	-1,298285928	3,71884E-05	0,021937162
ENSG00000271113	RP11-159H10.4	0,416214274	-1,264601652	5,0755E-07	0,00147939
ENSG00000112365	ZBTB24	0,421111515	-1,24772577	1,88817E-20	9,35608E-16
ENSG00000120675	DNAJC15	0,4545578	-1,137464341	4,32056E-05	0,023526151
ENSG00000213480	RP11-364P2.2	0,484195745	-1,046337694	5,86427E-09	4,37278E-05
ENSG00000256940	RP11-783K16.5	0,52099793	-0,940650455	0,000116923	0,04316744
ENSG00000236015	AC011290.5	0,52630168	-0,926038095	0,000000287	0,001016514
ENSG00000224274	ENSAP1	0,53524199	-0,901736796	2,67935E-05	0,018439527
ENSG00000165507	C10orf10	0,54564478	-0,873966047	1,02742E-08	6,36372E-05
ENSG00000254910	RP11-326C3.7	0,548888257	-0,86541562	0,000138315	0,045997476
ENSG00000220494	YAP1P1	0,558208854	-0,841123087	7,82227E-05	0,033340721
ENSG00000130066	SAT1	0,564614975	-0,824660701	2,14387E-05	0,016598569
ENSG00000260563	RP13-516M14.1	0,566027439	-0,821056104	1,48213E-06	0,002937647
ENSG00000247095	MIR210HG	0,571981543	-0,805959501	5,76607E-05	0,028288584
ENSG00000236182	RP11-297K7.1	0,575450831	-0,797235432	2,43288E-05	0,01753826
ENSG00000225770	AC092933.3	0,582534838	-0,779583763	6,17736E-09	4,37278E-05
ENSG00000167733	HSD11B1L	0,583448174	-0,777323583	2,78074E-05	0,018620084
ENSG00000143847	PPFIA4	0,584092594	-0,775731004	5,41691E-07	0,001491185
ENSG00000145293	ENOPH1	0,585854597	-0,771385448	2,87203E-07	0,001016514
ENSG00000229083	PSMA6P2	0,590486762	-0,760023378	0,00006528	0,029950838
ENSG00000230224	PHBP9	0,603938741	-0,727525875	0,000117608	0,04316744
ENSG00000186897	C1QL4	0,614348374	-0,702871109	9,62855E-05	0,038168359
ENSG00000254506	RP11-748H22.1	0,619001977	-0,691984077	4,62144E-05	0,024532999
ENSG00000232380	ZDHHC20P4	0,622162252	-0,684637229	1,60488E-05	0,014854462
ENSG00000176788	BASP1	0,623449344	-0,681655752	2,44221E-05	0,01753826
ENSG00000228986	RP13-228J13.8	0,624530743	-0,679155504	2,96195E-06	0,00456816
ENSG00000244153	WWP1P1	0,625151169	-0,677723003	9,31647E-07	0,002098365
ENSG00000142227	EMP3	0,626777792	-0,673974032	0,000001602	0,00305313
ENSG00000139921	TMX1	0,628377	-0,670297719	7,83921E-07	0,001849717
ENSG00000213290	PGK1P2	0,634386151	-0,656566818	4,91773E-05	0,024846568
ENSG00000237801	AMDP1	0,639994148	-0,643869382	5,45822E-06	0,006596589
ENSG00000131389	SLC6A6	0,64229385	-0,638694612	0,000000987	0,002126309
ENSG00000090054	SPTLC1	0,646719963	-0,628786952	4,71065E-06	0,005835434
ENSG00000230870	FBXW11P1	0,648540377	-0,624731698	0,000112513	0,042558399
ENSG00000236686	BZW1P1	0,651711446	-0,617694761	0,000151113	0,048621906
ENSG00000121966	CXCR4	0,65512456	-0,610158861	4,04265E-06	0,00527151
ENSG00000272520	CTD-2044J15.2	0,656889602	-0,606277165	0,000123013	0,043717729
ENSG00000122203	KIAA1191	0,663631161	-0,591546464	1,96077E-05	0,015596156
ENSG00000198406	BZW1P2	0,663736204	-0,591318126	3,52198E-05	0,021453568
ENSG00000254406	RP11-215D10.1	0,664082175	-0,59056632	1,89685E-05	0,015596156
ENSG00000266282	UBL5P2	0,664657609	-0,589316752	4,38366E-06	0,005569605
ENSG00000254682	RP11-660L16.2	0,665024554	-0,588520486	6,34857E-05	0,029399819
ENSG00000248015	AC005329.7	0,665050876	-0,588463385	0,000075332	0,03274365
ENSG00000169242	EFNA1	0,669841996	-0,578107265	4,08778E-05	0,022802697
ENSG00000141425	RPRD1A	0,672548701	-0,572289355	5,72511E-07	0,001493079
ENSG00000231549	USMG5P1	0,676331869	-0,564196759	2,63535E-05	0,018392137
ENSG00000232801	SDCBPP3	0,679462884	-0,55753335	0,000125842	0,04390957
ENSG00000214121	TDPX2	0,680475654	-0,555384548	1,98292E-05	0,015596156
ENSG00000261612	SUB1P3	0,683524585	-0,548934866	0,000137557	0,045997476
ENSG00000160408	ST6GALNAC6	0,688644251	-0,538169207	6,91152E-05	0,030853386
ENSG00000173674	EIF1AX	0,689250253	-0,536900202	6,15708E-05	0,029240244
ENSG00000249286	CTD-2210P15.2	0,693848208	-0,527308014	0,000114945	0,042824457
ENSG00000258445	RP11-307P22.1	0,693964876	-0,52706545	9,03382E-05	0,036994623
ENSG00000103449	SALL1	0,69616196	-0,522505111	5,27786E-05	0,026152313
ENSG00000270553	RP11-15E18.5	0,69719548	-0,520364879	0,000139701	0,046148875
ENSG00000157514	TSC22D3	0,697842351	-0,51902694	0,000029906	0,018998379
ENSG00000180730	SHISA2	0,698902817	-0,516836234	0,000121026	0,043514535
ENSG00000110218	PANX1	0,700723706	-0,513082391	0,00012818	0,044107264
ENSG00000221988	PPT2	0,701357405	-0,511778279	0,000124609	0,043790708
ENSG00000213409	RP11-658F2.3	0,701489017	-0,511507579	0,000111999	0,042558399
ENSG00000213684	LDHBP2	0,708015124	-0,498147917	0,000100621	0,038952261
ENSG00000006831	ADIPOR2	0,708029432	-0,498118763	8,82767E-05	0,036757985
ENSG00000130522	JUND	0,711466486	-0,491132295	2,95435E-05	0,018998379
ENSG00000257923	CUX1	1,365449977	0,449376462	0,000158375	0,049957002
ENSG00000133059	DSTYK	1,375898777	0,460374336	0,000123519	0,043717729
ENSG00000142156	COL6A1	1,38834809	0,473369329	0,000126719	0,04390957
ENSG00000116260	QSOX1	1,395197484	0,480469343	0,000121035	0,043514535
ENSG00000130363	RSPH3	1,42211213	0,508035222	0,000130535	0,044607681
ENSG00000196562	SULF2	1,422165478	0,508089341	0,000092847	0,037403769
ENSG00000183741	CBX6	1,425280114	0,511245483	1,41245E-05	0,01398908
ENSG00000241360	PDXP	1,425722878	0,511693588	0,000159295	0,049957002

Tabel S3: Proteins identified as ZBTB24 interactors by SILAC MS ordered by H/L

Label	Cell line
Light (L)	U2OS-GFP
Heavy (H)	U2OS-GFP-ZBTB24
Proteins with increased (SILAC ratio H/L ≥ 4) enrichment with at least 2 unique peptides	

Protein names	Gene names	Fasta headers	Peptides	Ratio H/L
Zinc finger and BTB domain-containing protein 24	ZBTB24	>sp|O43167|ZBT2	30	13,94
Zinc finger and BTB domain-containing protein 11	ZBTB11	>sp|O95625|ZBT1	2	11,32
Heat shock 70 kDa protein 1A/1B	HSPA1A	>sp|P08107|HSP7	25	7,57
60S ribosome subunit biogenesis protein NIP7 homolog	NIP7	>sp|Q9Y221|NIP7_	4	7,31
Pentatricopeptide repeat domain-containing protein 3, mitochondrial	PTCD3	>sp|Q96EY7|PTCI	11	7,22
Probable rRNA-processing protein EBP2	EBNA1BP2	>sp|Q99848|EBP2	9	7,06
Phospholipase DDHD1	DDHD1	>sp|Q8NEL9|DDH	22	6,98
Nucleolar complex protein 3 homolog	NOC3L	>tr|F5H677|F5H67	2	6,81
Guanine nucleotide-binding protein-like 3	GNL3	>sp|Q9BVP2-2|GN	5	6,79
ATP-dependent RNA helicase DDX54	DDX54	>sp|Q8TDD1|DDX	4	6,65
Putative ribosomal RNA methyltransferase NOP2	NOP2	>sp|P46087-2|NOI	11	6,36
Ribosome production factor 2 homolog	RPF2	>sp|Q9H7B2|RPF2	2	6,34
28S ribosomal protein S29, mitochondrial	DAP3	>sp|P51398-2|RT2	11	6,23
Pumilio domain-containing protein KIAA0020	KIAA0020	>sp|Q15397|K002(	7	6,22
Putative helicase MOV-10	MOV10	>tr|Q5JR04|Q5JR(	2	6,21
ATP-dependent RNA helicase DDX24	DDX24	>tr|F5GYL3|F5GYI	2	6,04
SHC SH2 domain-binding protein 1	SHCBP1	>sp|Q8NEM2|SHC	2	6,03
Ribosomal L1 domain-containing protein 1	RSL1D1	>sp|O76021|RL1D	15	6,00
Histone H3.2;Histone H3.1;Histone H3;Histone H3.1t;Histone H3.3;Histone H3.3C	HIST2H3A;HIST1H3A;H3F3B;H3F3A;HIST3H3;	>sp|Q71DI3|H32_I	7	5,98
Ribosome biogenesis protein BRX1 homolog	BRIX1	>sp|Q8TDN6|BRX	5	5,97
Ankyrin repeat domain-containing protein 17;Ankyrin repeat and KH domain-containir	ANKRD17;ANKHD1	>sp|O75179-6|ANI	4	5,86
Serine/threonine-protein phosphatase 6 regulatory subunit 3	PPP6R3	>tr|H7BXH2|H7BX	6	5,84
Histone H2A.V;Histone H2A.Z;Histone H2A	H2AFV;H2AFZ	>sp|Q71UI9|H2AV	3	5,83
Core histone macro-H2A.1	H2AFY	>sp|O75367-2|H2A	8	5,83
Procollagen-lysine,2-oxoglutarate 5-dioxygenase 3	PLOD3	>sp|O60568|PLOI	6	5,73
Histone H2B type 1-L;Histone H2B type 1-N;Histone H2B type 1-H;Histone H2B type	HIST1H2BL;HIST1H2BN;HIST1H2BH;HIST1H2	>sp|Q99880|H2B1	7	5,72
RRP12-like protein	RRP12	>sp|Q5JTH9-2|RR	6	5,69
Protein mago nashi homolog 2;Protein mago nashi homolog	MAGOHB;MAGOH	>tr|A6NEC0|A6NE	3	5,66
Cytoskeleton-associated protein 4	CKAP4	>sp|Q07065|CKAF	22	5,63
Methylosome protein 50	WDR77	>tr|B4DP38|B4DP:	2	5,59
Histone H1.1;Histone H1t	HIST1H1A;HIST1H1T	>sp|Q02539|H11_I	6	5,59
Histone H1.4;Histone H1.2;Histone H1.3	HIST1H1E;HIST1H1C;HIST1H1D	>sp|P10412|H14_I	9	5,59
Procollagen-lysine,2-oxoglutarate 5-dioxygenase 1	PLOD1	>sp|Q02809|PLOI	14	5,58
mRNA turnover protein 4 homolog	MRTO4	>sp|Q9UKD2|MRT	2	5,57
Protein KRI1 homolog	KRI1	>tr|H0YFD2|H0YFI	2	5,56
Histone H4	HIST1H4A	>sp|P62805|H4_H	11	5,52
Tripartite motif-containing protein 58	TRIM58	>sp|Q8NG06|TRI5	3	5,52
Ribonucleases P/MRP protein subunit POP1	POP1	>sp|Q99575|POP1	2	5,48
Growth arrest and DNA damage-inducible proteins-interacting protein 1	GADD45GIP1	>sp|Q8TAE8|G45II	2	5,45
BAG family molecular chaperone regulator 2	BAG2	>sp|O95816|BAG2	3	5,45
Protein SET	SET	>sp|Q01105-3|SET	2	5,43
Ribosome biogenesis regulatory protein homolog	RRS1	>sp|Q15050|RRS1	2	5,41
Nucleolar protein 16	NOP16	>tr|D6RIC3|D6RIC	2	5,39
E3 ubiquitin-protein ligase HERC2	HERC2	>sp|O95714|HERC	2	5,39
Heat shock cognate 71 kDa protein	HSPA8	>sp|P11142|HSP7(	27	5,36
Bystin	BYSL	>sp|Q13895|BYST	7	5,36
Importin subunit alpha-3	KPNA3	>sp|O00505|IMA4_	3	5,33
YTH domain-containing protein 1	YTHDC1	>sp|Q96MU7-2|YT	3	5,32
pre-rRNA processing protein FTSJ3	FTSJ3	>sp|Q8IY81|SPB1_	10	5,29
Histone H2B type 2-E;Histone H2B type 1-O;Histone H2B type 1-J;Histone H2B type	HIST2H2BE;HIST1H2BO;HIST1H2BJ;HIST3H2	>sp|Q16778|H2B2	7	5,28
Periodic tryptophan protein 1 homolog	PWP1	>tr|B4DJV5|B4DJV	4	5,28
Guanine nucleotide-binding protein subunit beta-2-like 1	GNB2L1	>sp|P63244|GBLP	11	5,27
Metastasis-associated protein MTA2	MTA2;DKFZp686F2281	>sp|O94776|MTA2	7	5,26
Melanoma-associated antigen B2	MAGEB2	>sp|O15479|MAGI	2	5,25
Poly [ADP-ribose] polymerase 1	PARP1	>sp|P09874|PARP	7	5,23
Prolow-density lipoprotein receptor-related protein 1;Low-density lipoprotein receptor-	LRP1	>sp|Q07954|LRP1	7	5,23
DnaJ homolog subfamily C member 9	DNAJC9	>sp|Q8WXX5|DNJ	2	5,15
Histone H2A type 2-B	HIST2H2AB	>sp|Q8IUE6|H2A2	4	5,13
Serine/threonine-protein kinase Nek7;Serine/threonine-protein kinase Nek6	NEK7;NEK6	>sp|Q8TDX7|NEK'	2	5,08
Probable ubiquitin carboxyl-terminal hydrolase FAF-X	USP9X	>sp|Q93008-1|USI	21	5,08
Histone H2A type 1-J;Histone H2A type 1-H;Histone H2A.J;Histone H2A type 2-C;His	HIST1H2AJ;HIST1H2AH;H2AFJ;HIST2H2AC;HI	>sp|Q99878|H2A1	6	5,07
Ankyrin repeat and SAM domain-containing protein 3	ANKS3	>tr|D3DUE4|D3DU	3	5,05
Putative ATP-dependent RNA helicase DHX30	DHX30	>sp|Q7L2E3-3|DH	17	5,02
RNA-binding protein 8A	RBM8A	>sp|Q9Y5S9|RBM	4	4,99
Chromobox protein homolog 3	CBX3	>sp|Q13185|CBX3	2	4,98
Protein AATF	AATF	>sp|Q9NY61|AATF	2	4,97
Eukaryotic initiation factor 4A-III	EIF4A3	>sp|P38919|IF4A3	8	4,95
Histone-binding protein RBBP4;Histone-binding protein RBBP7	RBBP4;RBBP7	>sp|Q09028-3|RBE	6	4,94
RNA-binding protein 34	RBM34	>tr|A2A2V2|A2A2\	3	4,93
Heterogeneous nuclear ribonucleoproteins C1/C2;Heterogeneous nuclear ribonucleo	HNRNPC;HNRNPCL1	>tr|G3V4W0|G3V4	10	4,92
Nucleolar RNA helicase 2	DDX21	>sp|Q9NR30-2|DD	11	4,89
78 kDa glucose-regulated protein	HSPA5	>sp|P11021|GRP7	23	4,87
Heterogeneous nuclear ribonucleoprotein U	HNRNPU	>sp|Q00839|HNRI	12	4,86
RNA-binding protein NOB1	NOB1	>tr|H3BUR4|H3BU	3	4,85
Y-box-binding protein 3	YBX3	>sp|P16989-3|YBC	9	4,83
Oxysterol-binding protein-related protein 3	OSBPL3	>sp|Q9H4L5-2|OS	2	4,77
N-acetyltransferase 10	NAT10	>sp|Q9H0A0|NAT1	8	4,76
Serine/threonine-protein phosphatase 6 regulatory ankyrin repeat subunit C	ANKRD52	>sp|Q8NB46|ANR5	4	4,76
Leucine-rich repeat-containing protein 1;Protein scribble homolog	LRRC1;SCRIB	>sp|Q9BTT6|LRRC	2	4,75
Serine/threonine-protein phosphatase 6 regulatory ankyrin repeat subunit A	ANKRD28	>sp|O15084-2|ANI	3	4,73
Histone H1.0	H1F0	>sp|P07305|H10_I	7	4,68
Melanoma-associated antigen C1	MAGEC1	>tr|A0PK03|A0PK(	2	4,68
Dedicator of cytokinesis protein 6	DOCK6	>sp|Q96HP0|DOC	15	4,67
Histone H1x	H1FX	>sp|Q92522|H1X_	3	4,66
Ribosome biogenesis protein BOP1	BOP1;KM-PA-2	>tr|E9PIF8|E9PIF8	2	4,64
Pinin	PNN	>sp|Q9H307|PININ	6	4,59
Protein arginine N-methyltransferase 5;Protein arginine N-methyltransferase 5, N-terr	PRMT5	>sp|O14744-2|ANI	6	4,55
RNA-binding protein PNO1	PNO1	>sp|Q9NRX1|PNO	4	4,54
Protein LTV1 homolog	LTV1	>sp|Q96GA3|LTV1	3	4,48
Heterogeneous nuclear ribonucleoprotein M	HNRNPM	>sp|P52272-2|HNI	6	4,45
Transformer-2 protein homolog beta	TRA2B	>sp|P62995|TRA2	7	4,43
Serine/arginine-rich splicing factor 6;Serine/arginine-rich splicing factor 4	SRSF6;SRSF4	>sp|Q13247-3|SRS	3	4,43

Tabel S4: Proteins identified as PARP1 interactors by SILAC MS ordered by H/L

Label	Cell line
Light (L)	U2OS-GFP
Heavy (H)	U2OS-GFP-PARP1
Proteins with increased (SILAC ratio H/L ≥ 2) enrichment with at least 2 unique peptides	

Protein names	Gene names	Fasta headers	Peptides	Ratio H/L
Zinc finger and BTB domain-containing protein 24	ZBTB24	>sp|O43167|ZBT24_HU	2	10,02
Poly [ADP-ribose] polymerase 1	PARP1	>sp|P09874|PARP1_HU	68	8,92
DNA polymerase beta	POLB	>tr|E7EW18|E7EW18_H	3	8,83
Bifunctional polynucleotide phosphatase/kinase;Polynucleotide 3-phosphatase;Polynu	PNKP	>tr|M0R3C8|M0R3C8_H	4	7,06
DNA repair protein XRCC1	XRCC1	>tr|F5H8D7|F5H8D7_HI	5	6,15
DNA ligase 3	LIG3	>sp|P49916|DNLI3_HUI	20	5,88
Chromodomain-helicase-DNA-binding protein 1-like	CHD1L	>sp|Q86WJ1-2|CHD1L_	3	5,85
Core histone macro-H2A.1	H2AFY	>sp|O75367-2|H2AY_HI	5	5,48
Histone H2B type 1-L;Histone H2B type 1-N;Histone H2B type 1-H;Histone H2B type	HIST1H2BL;HIST1H2BN;HIST1H2	>sp|Q99880|H2B1L_HU	5	5,14
Histone H2A.V;Histone H2A.Z;Histone H2A	H2AFV;H2AFZ	>sp|Q71UI9|H2AV_HUM	4	5,02
Histone H4	HIST1H4A	>sp|P62805|H4_HUMAI	9	4,92
Histone H3.2;Histone H3.1;Histone H3;Histone H3.1t;Histone H3.3;Histone H3.3C	HIST2H3A;HIST1H3A;H3F3B;H3F	>sp|Q71DI3|H32_HUMA	5	4,83
Histone H2B type 2-E;Histone H2B type 1-O;Histone H2B type 1-J;Histone H2B type	HIST2H2BE;HIST1H2BO;HIST1H	>sp|Q16778|H2B2E_HU	6	4,74
Histone H2A type 2-B	HIST2H2AB	>sp|Q8IUE6|H2A2B_HU	3	4,70
Histone H2A type 1-J;Histone H2A type 1-H;Histone H2A.J;Histone H2A type 2-C;Hist	HIST1H2AJ;HIST1H2AH;H2AFJ;H	>sp|Q99878|H2A1J_HU	4	4,40
Inosine-5-monophosphate dehydrogenase 2	IMPDH2	>tr|H0Y4R1|H0Y4R1_H	6	4,30
Heat shock 70 kDa protein 1A/1B	HSPA1A	>sp|P08107|HSP71_HU	14	3,51
DNA topoisomerase 2;DNA topoisomerase 2-alpha;DNA topoisomerase 2-beta	TOP2B;TOP2A	>tr|E9PCY5|E9PCY5_H	2	2,99
Ubiquitin-60S ribosomal protein L40;Ubiquitin;60S ribosomal protein L40;Ubiquitin-40S	UBB;RPS27A;UBC;UBA52;UBBP4	>tr|J3QS39|J3QS39_HU	2	2,83
Heat shock cognate 71 kDa protein	HSPA8	>sp|P11142|HSP7C_HU	16	2,76
Nuclease-sensitive element-binding protein 1	YBX1	>sp|P67809|YBOX1_HU	4	2,33
78 kDa glucose-regulated protein	HSPA5	>sp|P11021|GRP78_HU	13	2,32
Nucleolin	NCL	>sp|P19338|NUCL_HUM	5	1,94
Heterogeneous nuclear ribonucleoproteins C1/C2;Heterogeneous nuclear ribonucleop	HNRNPC;HNRNPCL1	>tr|G3V4W0|G3V4W0_H	2	1,94
Guanine nucleotide-binding protein subunit beta-2-like 1	GNB2L1	>sp|P63244|GBLP_HUM	4	1,92
Tubulin beta-4B chain	TUBB4B	>sp|P68371|TBB4B_HU	9	1,50
Tubulin alpha-1B chain;Tubulin alpha-1C chain	TUBA1B;TUBA1C	>sp|P68363|TBA1B_HU	8	1,23
Heterogeneous nuclear ribonucleoprotein U	HNRNPU	>sp|Q00839|HNRPU_H	2	1,21
Tubulin beta chain	TUBB	>tr|Q5JP53|Q5JP53_HU	10	1,17
ADP/ATP translocase 3	SLC25A6	>sp|P12236|ADT3_HUM	2	1,17
Tubulin alpha-3C/D chain;Tubulin alpha-3E chain	TUBA3C;TUBA3E	>sp|Q13748|TBA3C_HU	9	1,15
ADP/ATP translocase 2;ADP/ATP translocase 1	SLC25A5;SLC25A4	>sp|P05141|ADT2_HUM	2	1,13
Pyruvate kinase isozymes M1/M2;Pyruvate kinase	PKM;PKM2	>sp|P14618|KPYM_HUI	6	1,10
Clathrin heavy chain 1	CLTC	>sp|Q00610-2|CLH1_HI	2	1,03
Nucleophosmin	NPM1	>sp|P06748-2|NPM_HU	2	1,03
Galectin-1	LGALS1	>sp|P09382|LEG1_HUM	2	1,02
Heat shock protein beta-1	HSPB1	>sp|P04792|HSPB1_HU	2	0,97
Vimentin	VIM	>sp|P08670|VIME_HUM	10	0,91
LanC-like protein 2	LANCL2	>sp|Q9NS86|LANC2_HI	2	0,90
Elongation factor 1-delta	EEF1D	>sp|P29692-3|EF1D_HU	2	0,86
DNA replication licensing factor MCM3	MCM3	>sp|P25205|MCM3_HUI	5	0,83
Annexin A2;Annexin;Putative annexin A2-like protein	ANXA2;ANXA2P2	>sp|P07355|ANXA2_HU	15	0,80
Cystatin-B	CSTB	>sp|P04080|CYTB_HUM	2	0,80
Filamin-A	FLNA	>tr|Q5HY54|Q5HY54_H	2	0,80
ATP-dependent RNA helicase DDX3X;ATP-dependent RNA helicase DDX3Y	DDX3X;DDX3Y	>sp|O00571-2|DDX3X_I	3	0,79
Melanoma-associated antigen 4;Melanoma-associated antigen 8	MAGEA4;MAGEA8	>sp|P43358|MAGA4_HU	2	0,78
Heterogeneous nuclear ribonucleoprotein H;Heterogeneous nuclear ribonucleoprotein	HNRNPH1	>sp|P31943|HNRH1_HU	3	0,77
Endoplasmic reticulum resident protein 44	ERP44	>sp|Q9BS26|ERP44_HU	3	0,77
Glyceraldehyde-3-phosphate dehydrogenase	GAPDH	>sp|P04406-2|G3P_HUI	2	0,77
Profilin	PFN2	>tr|C9J0J7|C9J0J7_HUI	4	0,77
Peroxiredoxin-1	PRDX1	>sp|Q06830|PRDX1_HU	9	0,76
Phenylalanine--tRNA ligase beta subunit	FARSB	>sp|Q9NSD9|SYFB_HU	3	0,75
Cysteine and glycine-rich protein 2	CSRP2	>sp|Q16527|CSRP2_HU	5	0,74
Probable ATP-dependent RNA helicase DDX17	DDX17	>sp|Q92841-1|DDX17_H	4	0,74
Filamin-C	FLNC	>sp|Q14315-2|FLNC_HU	3	0,74
Crk-like protein	CRKL	>sp|P46109|CRKL_HUM	4	0,72
Putative elongation factor 1-alpha-like 3;Elongation factor 1-alpha 1	EEF1A1P5;EEF1A1	>sp|Q5VTE0|EF1A3_HU	8	0,72
CTP synthase 1	CTPS1	>sp|P17812|PYRG1_HU	6	0,72
Heat shock protein HSP 90-beta	HSP90AB1	>sp|P08238|HS90B_HU	5	0,71
Myosin-9	MYH9	>sp|P35579|MYH9_HUM	3	0,68
Probable ATP-dependent RNA helicase DDX5	DDX5	>sp|P17844|DDX5_HUM	5	0,65
Actin, cytoplasmic 2;Actin, cytoplasmic 2, N-terminally processed;Actin, cytoplasmic 1	ACTG1;ACTB;ACTA1;ACTC1;ACT	>sp|P63261|ACTG_HUM	12	0,65
Peptidyl-prolyl cis-trans isomerase A;Peptidyl-prolyl cis-trans isomerase	PPIA	>sp|P62937|PPIA_HUM	2	0,63
Cofilin-1	CFL1	>sp|P23528|COF1_HUM	4	0,62
Histone deacetylase 6	HDAC6	>sp|Q9UBN7|HDAC6_H	4	0,61
U2 small nuclear ribonucleoprotein A	SNRPA1	>sp|P09661|RU2A_HUM	5	0,58
Prohibitin-2	PHB2	>tr|F5GY37|F5GY37_HI	2	0,57
Protein RCC2	RCC2	>sp|Q9P258|RCC2_HUI	2	0,50
Ketosamine-3-kinase	FN3KRP	>tr|I3L2G3|I3L2G3_HUM	2	0,42
Thioredoxin	TXN	>sp|P10599-2|THIO_HU	2	0,41
Heterogeneous nuclear ribonucleoprotein A1;Heterogeneous nuclear ribonucleoprotei	HNRNPA1;HNRNPA1L2	>sp|P09651-3|ROA1_HU	3	0,32
Tubulin beta-3 chain	TUBB3	>sp|Q13509|TBB3_HUM	8	0,25
LanC-like protein 1	LANCL1	>tr|E9PHS0|E9PHS0_H	2	0,24
Keratin, type I cytoskeletal 17	KRT17	>sp|Q04695|K1C17_HU	4	0,21
Hornerin	HRNR	>sp|Q86YZ3|HORN_HU	5	0,19
Keratin, type II cytoskeletal 5	KRT5	>sp|P13647|K2C5_HUM	8	0,11
Keratin, type I cytoskeletal 14	KRT14	>sp|P02533|K1C14_HU	10	0,09
Keratin, type II cytoskeletal 6C;Keratin, type II cytoskeletal 6B;Keratin, type II cytoskel	KRT6C;KRT6B;KRT6A	>sp|P48668|K2C6C_HU	12	0,06
Keratin, type I cytoskeletal 16	KRT16	>sp|P08779|K1C16_HU	7	0,03
Keratin, type I cytoskeletal 9	KRT9	>sp|P35527|K1C9_HUM	7	0,03
Keratin, type II cytoskeletal 2 epidermal	KRT2	>sp|P35908|K22E_HUM	13	0,03
Keratin, type I cytoskeletal 10	KRT10	>sp|P13645|K1C10_HU	18	0,02
Keratin, type II cytoskeletal 1	KRT1	>sp|P04264|K2C1_HUM	22	0,02